



Review

Precise calculation of crystallite size of nanomaterials: A review



S.A. Hassanzadeh-Tabrizi

Advanced Materials Research Center, Department of Materials Engineering, Najafabad Branch, Islamic Azad University, Najafabad, Iran

ARTICLE INFO

Keywords:

Crystallite size
Nanomaterials
Scherrer method
Williamson-Hall method
Rietveld method

ABSTRACT

Crystallite size has an important effect on the chemical, physical and mechanical properties of metallic, polymeric, and ceramic nanomaterial. Therefore, finding a reliable method to calculate the crystallite size has been a hot debate in recent decades. Many direct and indirect measurement methods have been proposed. However, findings showed that some of them are reliable while others do not provide a good approximation. In the present review, a comprehensive study has been made to investigate these techniques, which are mainly based on X-Ray diffraction, Raman spectroscopy, and dark-field transmission electron microscopy. Scherrer method has been widely used as the easiest and fastest route to calculate crystallite size. However, most of the methods based on the peak broadening of XRD do not give information about the crystallite size distribution. In addition, some calculational and technical errors reduce the accuracy of measurement which should be corrected. Raman spectroscopy is also a suitable method that gives relatively accurate results. Although this method has been well documented for carbon-based nanomaterial, there are still some computational difficulties for the other nano-systems. An effective way for precise calculation of crystallite size is dark field TEM/HRTEM which provides both crystallite size and crystallite size distribution. However, this method provides information from a small area of surface, which is not representative of the entire sample. Therefore, due to the limitations of each method, a combination of these techniques may provide complimentary results which is the best strategy for an in-depth analysis of crystallite size, lattice strain and crystallite size distribution.

1. Introduction

A crystallite is a domain of solid-state matter that has the same structure with the same crystallographic orientation. Crystallites can vary in size from a few nanometers to several millimeters. This structure forms during synthesis, for instance, during the cooling and solidification or reaction. In other words, crystallite is a structural parameter. These structures are bonded together by irregular boundaries, forming a polycrystalline solid [1,2]. Crystallites with typical diameters between 1 and 100 nm make up nanocrystalline materials [3–6]. Conventional polycrystalline materials often have crystallite sizes that are many orders of magnitude bigger. In the nanocrystalline state, this difference may create unique or improved mechanical, magnetic, photocatalytic or transport capabilities [7–11]. The deviation from the norm for such behaviors depends sensitively on the crystallite-size distribution [12, 13].

The measurement of the crystallite size is as crucial as other characterization of material such as the determination of the crystalline phase, morphological description, and elemental composition. Controlling crystallite size is an essential fabrication aim since it may have a

significant impact on the qualities of materials [14–21]. For example, Upadhyay et al. [22] chemically synthesized iron oxide and investigated the structural and magnetic properties of samples via a transmission electron microscope, vibrating sample magnetometer and X-ray diffraction. Magnetic parameters of the specimens revealed a strong dependence on average crystallite size. The shift from a single domain to a multi-domain structure is predicted to occur at a diameter of order 36 nm for a magnetic crystallite. If the particle size is less than 14 nm, they exhibit superparamagnetic characteristics, and if the particle size is greater than 36 nm, they exhibit multi-domain features. Berkowitz and Schuele [23] also investigated the effect of crystallite size on the magnetic characteristics of γ -Fe₂O₃. Their study showed that saturation decreases with reducing crystallite size. The ratio of Hc(83 K)/Hc(293 K) grew significantly with reducing crystallite size while the room-temperature coercive force dropped. Iqbal et al. [24] prepared CuFe₂O₄ with different crystallite sizes by wet chemical methods. With increasing crystallite size, Curie temperature, dielectric loss tangent, dielectric constant, DC electrical resistivity, and hyperfine splitting of the samples changed.

The optical properties of materials also depend on the crystallite size

E-mail addresses: dralihassanzadeh@gmail.com, hassanzadeh@pmt.iaun.ac.ir.

[25–27]. For instance, it was suggested that the blue shift of the optical absorption edge was caused by the quantum size effect [28]. Makhlof et al. [29] prepared nickel oxide films with different crystallite sizes by post-annealing of Ni(OH)_2 in air. They reported that the crystallite increased with rising the calcination temperature. NiO nanostructured films with larger crystallite sizes have a shorter wavelength shift at the UV absorption edge.

Plasmonic effects were reported for noble metals like Au and Ag when their sizes were reduced to the nanoscale [30–33]. This phenomenon makes these nanomaterials very useful in the photocatalyst industry and increases the light-harvesting in the photosystems. Plasmonic effects are according to the collective oscillation of free charge carriers on the surface of noble nanocrystallites that are in resonance with photons in the visible light spectrum which produce hot electrons and holes [34–36].

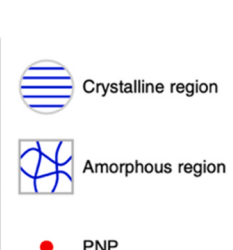
It is noteworthy that the definition of crystallites in polymers is different from what we know in ceramics and metals. In polymers, crystalline structures are related to the alignment of molecular chains instead of an ordered, three-dimensional arrangement of atoms in the structure, which is seen in ceramics and metals [37–39]. These chains fold together to create organized and ordered areas [40]. Therefore, the definition of crystallites in polymers is different from two other groups of materials. Nevertheless, the size and amounts of the crystalline phase affect the mechanical, optical, chemical, and thermal properties of the polymer [41–44]. In other words, the size and orientation of the molecular chains as well as the degree of crystallinity have an important role in determining the characteristics of the polymers. Lu et al. [45] adjusted the transport properties of the polymeric desalination membranes through the control of polymer crystallite size. Fig. 1 shows the procedure of the synthesis. In order to create modified membranes, pure

cellulose triacetate (CTA) samples were first soaked in a p-nitrophenol (PNP) solution and then rinsed with water. The areas with crystalline and amorphous structures are observed in the scheme. Since most of the polymeric chains are quenched in the polymer matrix, a skin layer made up of big crystallites embedded in amorphous areas is formed (Fig. 1a). PNP performs as a plasticizer in the CTA polymer and disperses inside the membrane (Fig. 1b). In particular, the partitioning of PNP molecules into the polymeric matrix improves chain mobility in the amorphous areas while simultaneously enlarging the crystalline domains. The PNP molecules that were integrated into the polymer film had a tendency to leak out when washed with water. The slow leaching process caused a rearrangement of polymeric chains to make smaller crystallites due to the interaction between CTA polymer and PNP via hydrogen bonding (Fig. 3c). Notably, smaller crystallites lead to a higher interfacial area between crystalline and amorphous areas since the total crystallinity of the deswelled specimen did not differ significantly from that of the pristine sample. The new structure with a smaller crystallite size would reduce nonselective mass transport routes, improving the water/salt selectivity of the sample.

As mentioned above, the fabrication and tuning of ceramic, metallic, and polymeric materials with specified properties require close control of crystallite size. One important issue is the techniques that could be used for the estimation of this value. Therefore, the aim of this review is to introduce and compare different methods with their accuracy and validity for the measurement of crystallite size in different categories of materials.

2. Crystallite versus particle

The question that always arises is whether crystallite and particle are



- Penetration of PNP**
- Induce plasticization
 - Destroy crystalline regions

Extraction of PNP

- Induce recrystallization
- Form smaller crystallites
- Enlarge interfacial area

Fig. 1. The mechanism for p-nitrophenol treatment role in the modification of the transport properties of the sample via manipulation of crystallite size. (a) The pure CTA sample is semi-crystalline, comprising of large crystallites embedded in amorphous regions. (b) Subjecting the sample to PNP solutions causes swelling of both the amorphous and crystalline regions. PNP increases the chain mobility of the polymeric matrix. (c) Removal of PNP by water rinsing causes rearrangement and recrystallization of the polymer chains. The interfacial area between the amorphous and crystalline regions is increased by this mechanism, which does not change the overall crystallinity but causes the development of smaller crystallites [45].

the same. The answer is that in special cases, the crystallite size and particle size may be the same, but in most cases, the crystallite size is not equal to the particle size. Fig. 2 shows a comparison between crystallite and particle. As can be seen, a particle could be amorphous, single-crystalline, or polycrystalline. An amorphous particle lacks a definite regular crystal structure and has no discernible long-range order in the arrangement of its atoms (Fig. 2a). Therefore, crystallite size is not meaningful in this condition, but particle size can be determined. Each of the several tiny areas in a polycrystalline particle has a well-organized structure, yet they are completely distinct from one another and are divided by grain boundaries (Fig. 2b) [46]. These regions are crystallites. In this case, the crystallite size could be estimated which is smaller than the particle size because several crystallites make a particle [47, 48]. In a single-crystal, all the atoms are arranged in an orderly array and there are no grain boundaries (Fig. 2c). As can be seen when the particle is a single-crystal, the size of the crystallite is equal to the particle size. Since the formation of particles and crystallites are dependent on nucleation and growth kinetics during synthesis processing, their sizes may be different or equal because of the condition of synthesis and the nature of the material. For example, in glass powders, there is no crystal structure (no crystallites), but there is particle size. In most of the reported studies, the crystallite size is smaller than the particle size. This difference may be due to two main reasons. First, the produced particles are polycrystalline. In this case, the particle size calculated by TEM analysis is several times larger than the measured crystallite size. The second reason is that the researchers do not provide a correction on their obtained results which are used for the calculation of crystallite size. For

instance, the Scherrer method underestimates the size of the grain because it ignores the widening of the diffraction peaks caused by the microstrain of the lattice [49,50]. This can cause errors in the estimated crystallite size results. Therefore, in the present review, we try to investigate different methods of crystallite size measurement which have the least error.

3. Particle size

Several ways were reported for the particle size calculation. Microscopic methods like TEM in bright-field mode and SEM may be the most famous direct routes for studying ceramic, metallic and polymeric nanomaterials [51–56]. Indirect ways like BET have also been used for particle size measurement through the determination of specific surface areas. For this aim, Eq. 1 has been utilized by many researchers [57–60].

$$D = \frac{A}{Sp} \quad (1)$$

where D is the average particle diameter, S is the specific surface area (m^2/g), and ρ (g/cm^3) is the density of nanoparticles. A is a shape factor that is 6000 for spherical particles. The difference between the obtained particle size from BET and TEM can give valuable information about the degree of powder agglomeration. It has been reported that if the particle size calculated from TEM is larger than that obtained from BET, the powders are agglomerated [61]. Dynamic light scattering (DLS) is a useful method for investigating particle size and distribution of colloidal nanoparticles [62]. In addition, a simple technique for calculating the

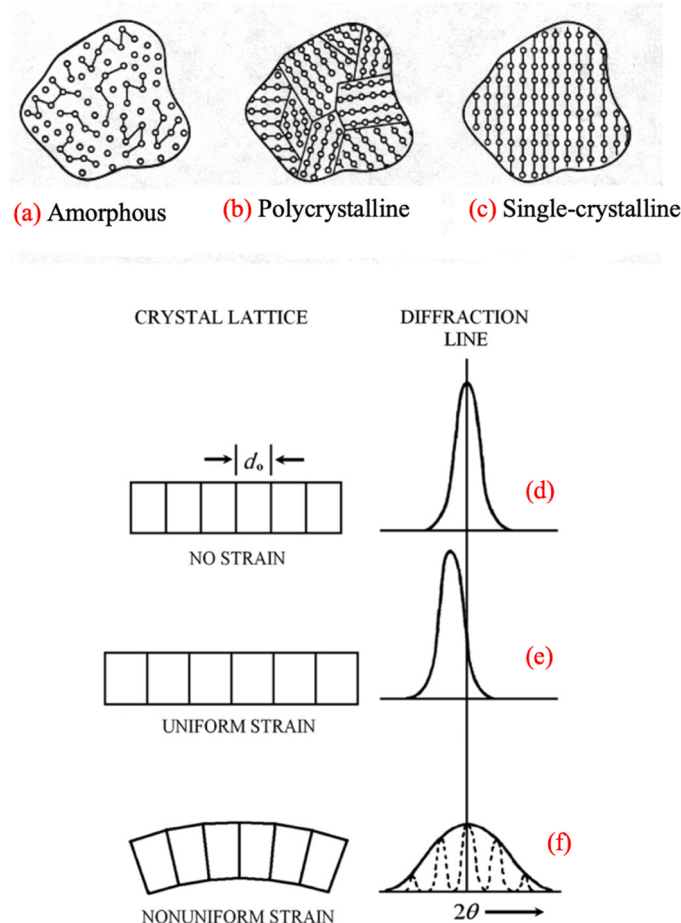


Fig. 2. General classification of particles based on the crystal structure: (a) amorphous, (b) polycrystalline, and (c) single-crystalline. Effect of strain on the XRD peaks: (d) unstrained grains, (e) uniform tensile strain, and (f) nonuniform strain. The uniform strain affects the peak position and the nonuniform strain affects the peak broadening and intensity [86].

diffusion coefficient and, consequently, the hydrodynamic radius of nano-objects is Taylor Dispersion Analysis (TDA) [63]. This method resembles DLS which gives particle size in a colloidal solution [64]. Malburet et al. [65] used TDA as a new methodology for the characterization of the size and polydispersity of lipid nanoparticles as carriers for mRNA vaccines. They showed that this method is reliable for the investigation of particle size and dispersity. However, most of these analytical methods are not suitable for crystallite size measurement and are more useful for particle size study.

4. Crystallite size

In order to determine the size of the crystallites in nanocrystalline materials, there are two main methods: direct imaging, such as dark-field transmission electron microscopy (DFTEM), and indirect measurement, such as X-ray diffraction or Raman spectroscopy. Each of these approaches has its own advantages and disadvantages. For example, direct imaging has the ability to reveal the complete distribution of crystallite sizes in a sample, although sample preparation and image processing are time-consuming and frequently difficult. In addition, a true area of the sample may not have been analyzed since the volume that may be examined under a microscope is usually quite tiny in relation to the full sample. On the other hand, indirect methods are fast and easy, but they usually give average crystallite size rather than the entire crystallite-size distribution, which is not very accurate. In addition, the sources of error in indirect measurement are higher which makes them more unreliable. In the following, these methods are reviewed and the corrections applied to them will be discussed.

4.1. Calculation based on X-ray diffraction method

As it is known, X-ray diffraction (XRD) has been widely used for structural analysis in materials for phase analysis [66–68] and for investigating the crystallinity of the product [69–71]. In addition to the main application of XRD, this method may be the most common way of determining crystallite size because of its simplicity [72,73]. The basis for this calculation is that smaller crystallites create wider and broader peaks [74,75]. In its most basic explanation, the Bragg condition is less strictly enforced in small crystallites because repeating lattice planes are fewer in this situation. As a result, X-rays with a wider angle are reflected without being suppressed by destructive interference effects [2, 76,77]. There is considerable debate over the maximum size at which crystallites may be measured using XRD. The XRD technique is believed to be suitable for crystallite sizes of up to 100 nm [58,78]. Guinier [79] reported that the largest size value of crystallites that may be calculated by X-ray diffraction is influenced by the wavelength of the X-ray tube and the angular location of the diffraction peak. Guinier reported that even with the best equipment, it is difficult to determine crystal sizes higher than 100–200 nm with excellent precision when using an X-ray tube with a copper target.

An ideal unit cell shows symmetrical, narrow, delta-function-like diffraction peaks. Peak broadening, peak shift, anisotropic peak broadening, and peak asymmetries are examples of deviations from the ideal powder pattern in a real sample. Peak broadening is a sign of crystallite smallness, micro-strain and micro-stresses, although it can be due to chemical heterogeneities, stress gradients and instrumental effects [80]. Peak shift can be seen in the samples with a solid solution, adding a dopant element, etc. [81–85]. Therefore, these changes can be considered as a tool to analyze the structure. The lattice flaws prevent the

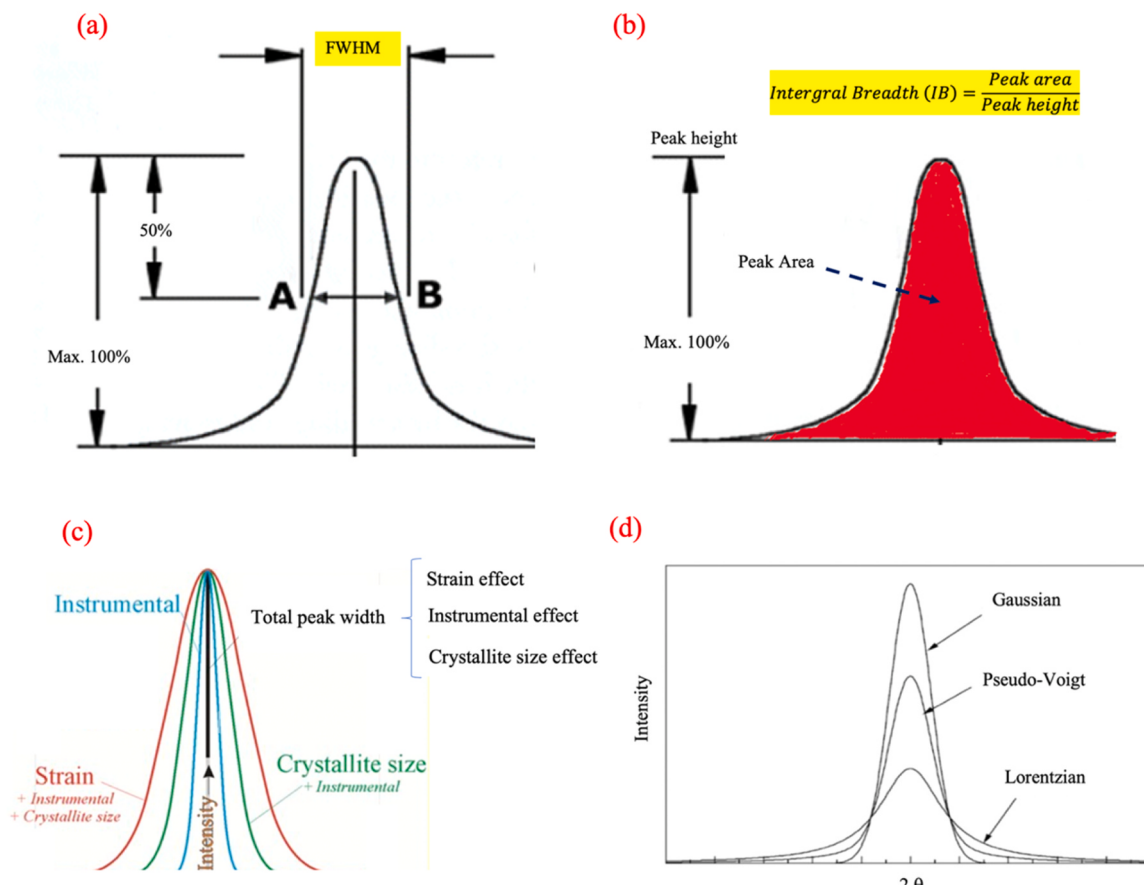


Fig. 3. Determination of (a) FWHM and (b) IB of an XRD peak. (c) Effect of different parameters on the width and area of an XRD peak which comprise instrument and sample-dependent effects. (d) Gaussian, Pseudo-Voigt and Lorentzian functions.

material from being completely crystalline and also cause stresses to develop in the lattice due to variations in the lattice constants. In addition, other parameters such as instrumental interference, stacking faults, etc. also affect the peak width in XRD which should be considered for precise calculation of the crystallite size [86–89]. The effect of strain on the XRD peaks is shown in Fig. 2. As can be seen, nonuniform strain affects the peak broadening and intensity, whereas uniform strain affects the peak position [86].

Based on the above discussion it can be concluded that the peak width in the XRD patterns arises from different sources that one of them is crystallite size. Therefore, for precise estimation of crystallite size, some modifications to the peak width should be made.

4.1.1. Determination of the full width at half maximum or integral breadth

The first step for calculating crystallite size via the XRD method is determining the correct full width at half maximum (FWHM) or integral breadth (IB) from XRD peaks as shown in Fig. 3a and b. Both FWHM and IB have been used in the literature for the calculation of crystallite size.

FWHM is the width of a spectrum curve measured between the background and the peak maximum (Fig. 3a). It can be obtained through X'Pert HighScore software or by fitting data via curve drawing software like origin pro, sigma plot, etc. As mentioned before, the width of the diffracted peaks is a combination of both sample-dependent and instrument effects (Fig. 3c). This instrumental broadening in the XRD peaks arises from x-ray penetration in the sample, slit width, imperfect monochromaticity, and imperfect focusing. It is important to gather a diffraction pattern from the line broadening of a reference sample to estimate the instrumental widening in order to decouple these contributions. Large silicon particles might be a reference sample [90]. Coarse particles of the same sample material can also be used. For instance, Weibel et al. [58] used a standard microcrystalline rutile sample with a particle size of about 2 μm to calculate the crystallite size of nano TiO₂. They reported that this size is large enough to ignore particle size and microstrain broadening. Then, the peak broadening from the sample (FWHM_{sample}) should be subtracted from that of the instrument (FWHM_{instrument}) to calculate the correct peak width (FWHM_{corrected}) [91,92]. Lorentzian or Gaussian mathematical profiles are often utilized to deconvolute instrumental and size effects. These mathematical profiles are presented as Cauchy (Eq. 2) and Gauss approximation (Eq. 3) [93,94]. Both Gauss and Cauchy estimates are used in the literature for amending the FWHM.

$$FWHM_{corrected} = FWHM_{sample} - FWHM_{instrument} \quad (2)$$

$$(FWHM_{corrected})^2 = (FWHM_{sample})^2 - (FWHM_{instrument})^2 \quad (3)$$

While in some research better correlation was reported for the Cauchy approximation [58], Gaussian approximation has been used and approved more in literature. Therefore, in the first step, the FWHM should be amended to increase the accuracy of the calculation [95]. After this correction, the obtained FWHM can be used as an important parameter in different methods of crystallite size estimation which will be reviewed in the next sections.

Integral breadth (IB) that was proposed after the FWHM approach is based on the calculation of the area under a peak. The calculated area is then divided by peak height to obtain integral breadth. The area of a peak is usually calculated by fitting the data in an appropriate software like Origin Pro. The correction of the obtained IB value is also necessary to reduce the error originating from the instrument. These corrections are carried out like the FWHM method. It is worth mentioning that although the IB method is a newer approach used for the calculation of crystallite size, there are some reports in the literature about more accuracy of FWHM approach. For instance, Bakshi et al. [96] used both FWHM and IB methods for investigating the anisotropic broadening of XRD peaks of shear-deformed martensite. Modified Williamson-Hall and Warren-Averbach analyses were used as models to calculate crystallite

size and strain. They reported that when IB was taken into account for size and strain analysis, particularly for higher peak angles, the study has significant perturbation. In contrast, FWHM demonstrated rather excellent agreement with the aforementioned models. It seems that it is not possible to declare which approach is better. In other words, these approaches should be applied case by case to check which one provides more accurate results. For example, IB approach is not accurate when there is a lot of overlap between peaks in the XRD pattern because it is hard to determine where the tail of the peak ends and where the background begins. Therefore, the calculation of the peak area is not accurate in such a situation.

As mentioned before, both FWHM and IB can be obtained by fitting the data in graphing and data analysis software. For this aim, several stages should be done. First, the background of the peak should be defined. Second, obtained peaks are fitted with a series of equations. There are different functions like Gaussian, Lorentzian, etc. that can be applied. Some of these functions were shown in Fig. 3d. These functions usually exist in the database of the software. Higher fitness is more desirable. For example, many researchers used the Gaussian function [97–99]. However, some believe that the pseudo-Voigt function which has a profile between Gaussian and Lorentzian (Fig. 3d) is more appropriate for data fitting for XRD patterns [1,100,101]. Some researchers tried to use techniques that deconvolute the Gaussian and Lorentzian contributions to each diffraction peak which is very difficult. Pearson VII function also was used for fitting [102–105]. After finding the best fit, the required parameters (FWHM or IB) can be obtained from the used function. However, as mentioned before, obtained values should be modified to remove the instrumental error.

4.1.2. Scherrer method

The Scherrer technique, which ignores strain contribution to peak broadening, is the simplest and most used method for determining crystallite size from an XRD pattern [106–108]. This approach also can be applied to the crystallite size calculation of thin films [109–111]. According to this method (Eq. 4), the crystallite size (d) can be estimated [9,112–114].

$$d = \frac{K\lambda}{\beta \cos\theta} \quad (4)$$

where λ is the X-ray wavelength, β is the corrected FWHM or IB which is in radian, θ is the Bragg angle (degree) and K is the Scherrer constant. It should be emphasized that the unit of β (FWHM or IB), which is obtained from XRD patterns is in degrees and must be converted to radians before being used in the Scherrer formula. It was reported K value depends on the crystal shape, the diffraction line indexes, and the dispersion of crystallite sizes of the powder [1,115]. K is normally between 0.62 and 2.08 [2,116,117] and between 0.9 and 1 for spherical particles or the absence of any knowledge of the shape of crystallites [86,94,118–120]. The unit of d would be the same as the unit of λ . One restriction in this formula is that one peak is usually used for calculation. Nevertheless, in the cases where crystallite growth happens in one direction, this method is an asset that let us measure this oriented growth. However, some researchers utilized an average crystallite size from the d values obtained from each peak. In other words, the d values for all the peaks are calculated and then an average amount from all the results is obtained. However, it was reported that with the increase of diffraction angle, the accuracy of β reduces. It means that the accuracy of the calculated crystallite size for the peaks at high angles is lower than those measured at lower angles [121]. Therefore, taking an average from all d values reduces the accuracy of the measurement.

The least-square approach was employed to diminish the sources of errors. There have been lots of attempts to modify the Scherrer method using the least-square approach instead of taking an average. For instance, a straight-line model was proposed for the calculation of the crystallite size [122,123]. According to the Scherrer equation with some

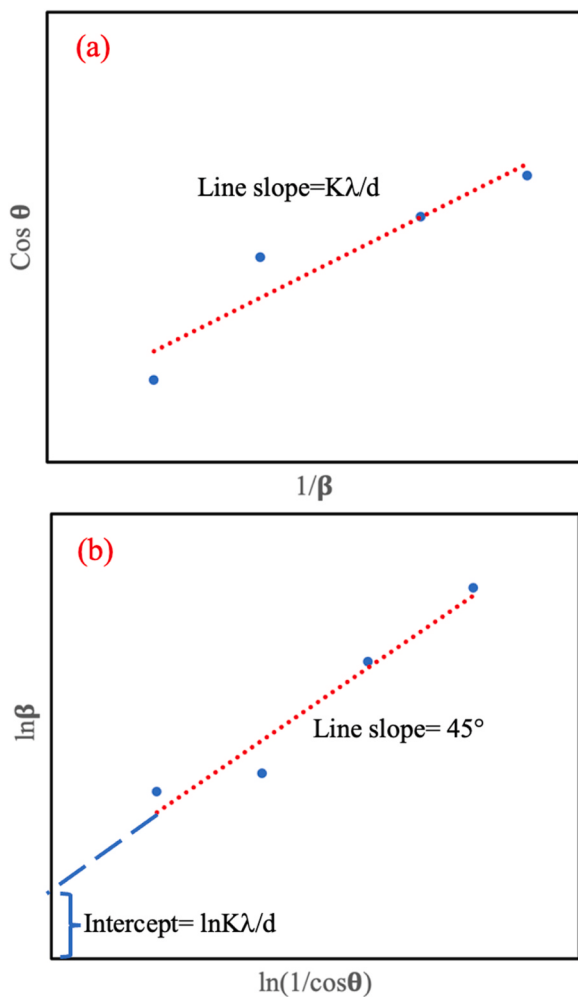


Fig. 4. Crystallite size calculation via Scherrer method based on (a) straight line style and (b) logarithmic approach.

displacements in its components (Eq. 5), a plot of $\cos \theta$ (θ in degree) versus $1/\beta$ (β in radian) could be drawn from the peaks and a straight line should be fitted from the results (Fig. 4a).

$$\cos \theta = \frac{K\lambda}{d} \cdot \frac{1}{\beta} \quad (5)$$

The slope of the fitted line is equal to $\frac{k\lambda}{d}$. However, it was reported that the obtained crystallite size from this method is not accurate and it is far from reality most of the time [122]. Therefore, it seems that the straight-line model is not an efficient modified approach for a precise calculation method of crystallite size. In addition, a modification to the Scherrer equation was carried out by Monshi et al. [121] to use all the peaks for measuring the crystallite size value (d). For this aim, a natural logarithm (\ln) is taken from each side of Eq. 4, as shown in Eq. 6.

$$\ln \beta = \ln \frac{k\lambda}{d} + \ln \frac{1}{\cos \theta} \quad (6)$$

By plotting the results of $\ln \beta$ against $\ln(1/\cos \theta)$ for different peaks, the intercept gives $\ln \frac{k\lambda}{d}$ (Fig. 4b). Therefore, it is possible to calculate the d value from the intercept of the fitted line. This modification also has the advantage of the use of all peaks for the crystallite size calculation. However, the main drawback of this method is that the slope of the fitted line must be equal to 1 (45°) to get a precise estimation which is almost impossible in practical use. Rabiei et al. [122] compared this modification method with straight-line model modification for crystallite size measurement of hydroxyapatite obtained from cow, pig, and chicken

bones. They reported that the Monshi modification method gives more accurate results than the straight-line model.

As mentioned before there is an upper limit to the crystallite size that can be estimated by the Scherer method. An instrumental effect has been reported that leads to such a limitation. However, there is controversy regarding the maximum size that can be calculated through this method. For instance, Holzwarth and Gibson [124] reported that because peak broadening reduces with rising crystallite size and it becomes challenging to distinguish the peak broadening caused by crystallite size from the broadening caused by other factors, this formula can be used for crystallite sizes up to 100–200 nm. Cullity et al. [125] recommended that the maximum application range of this method is about 200 nm due to the limitations of the diffractometer resolution. Muniz et al. [118] believed that the Scherrer equation can be applied to the sample with an upper limit of 600–1000 nm based on the position of the peak. In another study, He et al. [126] calculated the crystallite size of the silicon film and reported that the maximum applicable scope is 137 nm. These differences arise from the reason that the upper limit depends on the sample, instrument, and signal-to-noise ratio. For example, the applicable range of this method rises with the increasing diffraction angle. The linear absorption coefficient (μ_0) and Bragg angle (θ_B) are two important factors that affect the upper limit range so that this maximum is proportional to $\sin(\theta_B/\mu_0)$ [127]. In addition, the FWHM induced by the device itself typically falls between 0.06 and 0.09 in range. However, the FWHM of a monocrystal specimen is much lower than 0.06. Therefore, if the FWHM induced by the physical widening is lower than that caused by the instrumental broadening, the Scherrer equation will be less accurate. The instrumental broadening originates from the voltage of the X-ray tube and the slit width comprising receiving slit, divergence slit and receiving slit sola [126].

Pérez-Zúñiga et al. [128] produced a reduced graphene oxide/zinc oxide composite via a hydrothermal process. They used the Scherrer method for the calculation of both crystallite size and the number of reduced graphene oxide sheets. It was reported that the diffraction peak related to (022) of graphite planes changed from 26.6° to $\sim 11^\circ$ after the graphite oxidation process showing an increase in the interplanar distance due to entering oxygen in the structure. The opposite of the oxidation stage, the reduction process causes a decrease in the diffraction peak angle of (002) planes to 22° which is close to the original graphite diffraction peak indicating a reduction of the interplanar distance of (002) planes with the removal of oxygen from the lattice. They used the Scherrer formula (Eq. 4) for the calculation of crystallite size. Then, the obtained crystallite size was used for the estimation of the number of graphene sheets. For this aim, based on $GOS=L/d_{(002)}+1$ equation and using the crystallite size (L) calculated from the Scherrer formula and the d spacing of (002) value estimated from the XRD pattern, it is possible to determine the approximate number of graphene oxide sheets (GOS). Their findings demonstrated that the average crystallite size and $d_{(002)}$ for graphene oxide and reduced graphene oxide are 20 nm and 4 Å and 40 nm and 8.45 Å, respectively. As a result, both materials have roughly 6 layers of carbon.

Goktas et al. [129] synthesized ZnO and cobalt-doped ZnO thin film and investigated the effect of cobalt doping on the crystallite size. They used the Scherrer method for calculating crystallite size. It was found that cobalt doping reduces the crystallite size of zinc oxide. The reduction in crystallite size was attributed to the lattice distortion and formation of the defects or impurities in the structure of zinc oxide due to the doping process.

Yang et al. [130] produced nanosized SnSe via a wet chemical method and investigated the effect of pH on the crystallite size of samples based on the Scherrer equation. They reported increasing in the pH of the synthesis procedure from 1.4 to 12.3, resulting in an increase in crystallite size from 36.61 nm to 64.75 nm.

Mahajan et al. [131] synthesized manganese-doped cobalt-zinc spinel ferrite via sol-gel combustion method. They used the Scherrer formula for investigating the effect of Mn doping on the crystallite size of

cobalt-zinc spinel ferrite. The XRD peak with maximum intensity was utilized to obtain FWHM. The obtained crystallite size (D) was utilized to estimate dislocation density (δ) based on $\delta = 1/D^2$ equation. Therefore, crystallite size can give indirect information about the dislocation density of a sample which may be interesting for the researchers working on mechanical alloying of nanomaterials. Their results showed that the crystallite size first decreases with the Mn addition and then it increases and finally reduces. They believed that this irregular relationship between the crystallite size and the manganese content indicates that divalent or trivalent metal cations are present randomly in the tetrahedral and octahedral locations of the spinel ferrite structure. Therefore, the synthesized spinel ferrite breaks into random particles with different sizes and morphologies due to the inhomogeneous strain caused by the randomness distribution of metal cations.

Wu et al. [132] fabricated W-doped ZnFe₂O₄ composite nanofibers as acetone sensors. They used the Scherrer formula to calculate the crystallite size. It was found that with an increase in W doping the crystallite size decreases. The substitution of tungsten ions for iron ions in the structure of spinel ferrite causes a retarding force on the crystal boundaries, which prevents the movement of these boundaries and reduces crystallite size.

It is worth noting that the Scherrer method was also applied to polymeric materials for the calculation of crystallite size. Ali [133] investigated the optical and structural properties of polyvinyl alcohol/polyvinyl pyrrolidone/copper ions (PVA/PVP/Cu²⁺) composite. The crystallite length (D) of the PVA in the samples was measured with the Scherrer formula. It was reported that the D values of the composite samples are found to be substantially less than those of pure PVA. This study provided clear evidence that the degree of crystallinity decreases as a result of PVA spherulite size disruption caused by its complexation with PVP and copper ions.

Although Scherrer's basic formula is applied to each peak separately, which many consider a disadvantage, it is sometimes an advantage and provides valuable information about preferential crystallite growth. Kaur et al. [134] synthesized NiSe@MoSe₂ nanosystem via a hydrothermal method. They measured the crystallite size via the Scherrer formula for different peaks. The crystallite size was 166.0 nm, 30.9 nm, 13.1 nm and 9.1 nm for 34.0°, 45.4°, 50.7° and 62.5° reflection peaks, respectively. They believed that preferential crystal growth happens in their samples. In other words, the atoms are more densely packed onto the crystallographic planes with lower Miller indices, which results in lower free energy and a higher growth rate. This may be the reason for the higher crystallite size of the reflection peak at 34.0°. In addition, the crystals that develop close to or on the surface typically crystallize more quickly and are smaller as a result. In the core, crystals tend to be formed more slowly and grow larger. Therefore, based on the above discussion it can be concluded that measurement of crystallite size via the Scherrer method for each peak can be used as tools to investigate the preferential growth of crystallites.

4.1.3. Williamson-Hall method

One weakness of the Scherrer method is that it relates the peak width only to the size of the crystallites. While the width of the peaks depends not only on the size of the crystallites but also on the strain of the lattice [135–138]. This strain is formed in the structure due to different kinds of defects like point defects, grain boundaries, stacking faults, etc. [139, 140]. Williamson-Hall (W-H) method was used to cover all these parameters and gives a better estimate of the crystallite size [141–143]. In the W-H method, the broadening is deconvoluted into crystallite size and the lattice strain as shown in Eq. 7.

$$\beta_{\text{Sample}} = \beta_{\text{Crystallite size}} + \beta_{\text{Lattice strain}} \quad (7)$$

Three distinct models—uniform deformation model (UDM), uniform stress deformation model (USDM), and uniform defect energy density model (UDEDM)—are created via altering the W-H approach in

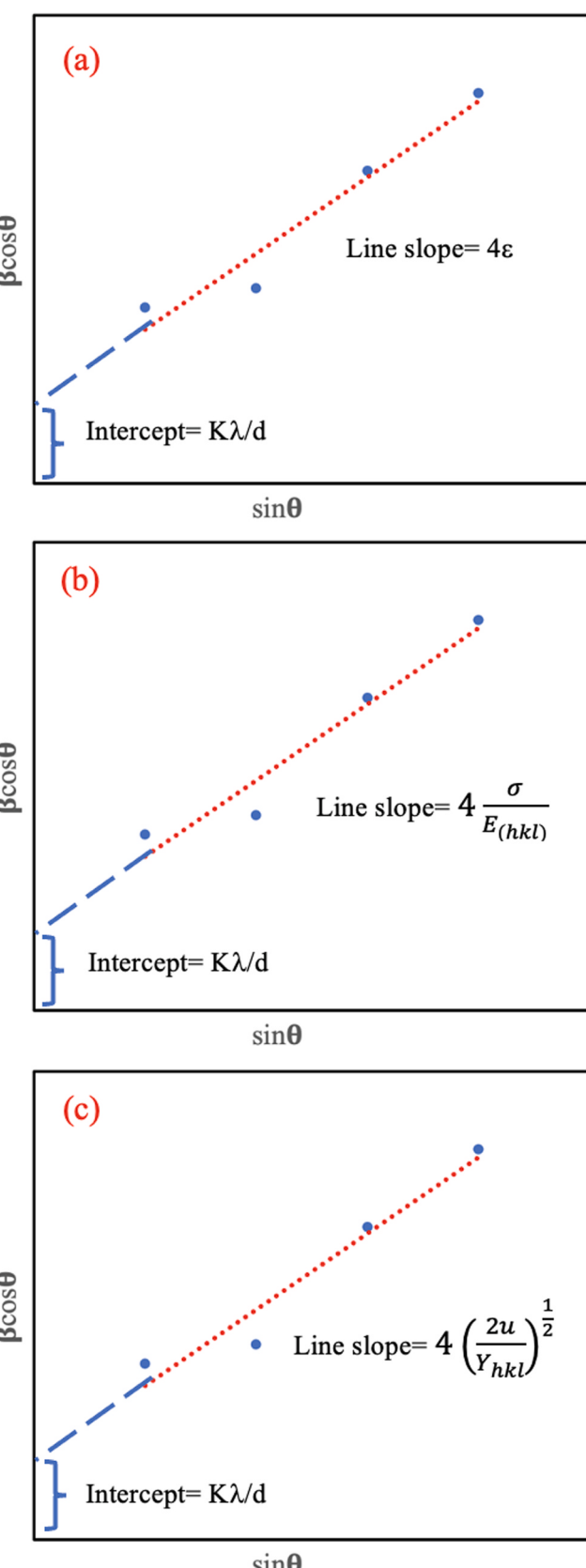


Fig. 5. Crystallite size and strain calculation via Williamson-Hall method based on (a) UDM, (b) USDM, and (c) UDEDM approaches.

accordance with different assumptions. The most commonly used form of the W-H route is the uniform deformation model. In UDM the $\beta_{\text{Crystallite size}}$ and $\beta_{\text{Lattice strain}}$ were obtained by Eqs. 8 and 9, respectively.

$$\beta_{\text{Crystallite size}} = \frac{K\lambda}{d\cos\theta} \quad (8)$$

$$\beta_{\text{Lattice strain}} = 4\epsilon\tan\theta = 4\epsilon \frac{\sin\theta}{\cos\theta} \quad (9)$$

where ϵ is lattice strain. According to Eqs. 7, 8 and 9, the W-H equation could be obtained (Eq. 10).

$$\begin{aligned} \beta_{\text{Sample}} &= \beta_{\text{Crystallite size}} + \beta_{\text{Lattice strain}} = \frac{K\lambda}{d\cos\theta} + 4\epsilon \frac{\sin\theta}{\cos\theta} \Rightarrow \beta_{(hkl)}\cos\theta \\ &= \frac{K\lambda}{d} + 4\epsilon\sin\theta \end{aligned} \quad (10)$$

By plotting $\beta_{(hkl)}\cos\theta$ against $\sin\theta$ ($\beta_{(hkl)}$ in radian and θ in degree) for all the peaks and fitting the best line, the intercept and slope the fitting line are $\frac{K\lambda}{d}$ and 4ϵ , respectively (Fig. 5a). Therefore, both crystallite size and strain can be estimated. Sometimes the intercept of the fitted line lies in negative values. Some researchers believe that the negative value for strain is meaningless, whereas others assert that it means compression strain in the sample [144,145]. The latter researchers believe that the positive value for intercept means tensile strain.

In the uniform stress deformation model the anisotropic nature of Young's modulus (E) is considered. It was reported that this approach is more consistent with reality [146,147]. According to Hooke's law, the relationship between stress and strain is proposed in Eq. 11 where the material is in the elastic region [148].

$$\sigma = E\epsilon \quad (11)$$

Therefore, the modified equation can be obtained by substitution the strain with $\frac{\sigma}{E}$ in Eq. 10 as shown in Eq. 12.

$$\beta_{(hkl)}\cos\theta = \frac{K\lambda}{d} + 4 \frac{\sigma}{E_{(hkl)}} \sin\theta \quad (12)$$

where E_{hkl} is Young's modulus in the direction perpendicular to the set of the crystal lattice plane. It means that strain is different in different crystal directions. The stress is calculated by fitting a line in the plot of $\beta_{(hkl)}\cos\theta$ versus $\sin\theta$ (Fig. 5b). Mostly, E_{hkl} values of materials are tabulated in the literature. Nevertheless, the E_{hkl} for cubic and hexagonal crystals can be measured from Eqs. (13) and (14), respectively [149].

$$\frac{1}{E_{hkl}} = S_{11} - 2 \left[\left(S_{11} - S_{12} - \frac{1}{2}S_{44} \right) \right] \left[\frac{h^2k^2 + k^2l^2 + l^2h^2}{(h^2 + k^2 + l^2)} \right] \quad (13)$$

$$E_{hkl} = \frac{\left[h^2 + \frac{(h+2k)^2}{3} + \left(\frac{al}{c} \right)^2 \right]^2}{S_{11} \left(h^2 + \frac{(h+2k)^2}{3} \right) + S_{33} \left(\frac{al}{c} \right)^4 + (2S_{13} + S_{44}) \left(h^2 + \frac{(h+2k)^2}{3} \right) \left(\frac{al}{c} \right)^2} \quad (14)$$

where S_{ij} , and C_{ij} are introduced as elastic compliances and elastic stiffness constants of material, respectively which could be earned from the literature.

The uniform deformation energy density model is also based on the assumption that Young's modulus is anisotropic. Eq. 15 can be used to get the energy density or energy per unit (u) for an elastic system that obeys Hooke's law.

$$u = \frac{(\epsilon^2 Y_{hkl})}{2} \quad (15)$$

Therefore, the W-H model can be rewritten according to the energy and Young's modulus (Eq. 16).

$$\beta_{hkl}\cos\theta = \left(\frac{k\lambda}{D} \right) + \left(4\sin\theta \left(\frac{2u}{Y_{hkl}} \right)^{\frac{1}{2}} \right) \quad (16)$$

Plots of $\beta_{hkl}\cos\theta$ versus $\sin\theta$ can be constructed, and fitted lines are drawn. The slopes of the lines are utilized to determine the anisotropic energy density (u), and their y-intercepts can be used to estimate the crystallite size (D). (Fig. 5c). After the calculation of energy, the stress and strain can be estimated from Eq. 15 and Eq. 11 (Hooke's law), respectively.

Nakasawa et al. [150] produced chromium disilicide via reduction-diffusion and spark plasma sintering techniques. They used the Williamson-Hall plot (uniform deformation model) for calculating of crystallite size of samples. It was reported that with the reduction in crystallite size, the lattice thermal conductivity of the SPS-treated chromium disilicide samples decreases. This decrease was attributed to the phenomenon that the nanocrystallites inhibit the propagation of phonons with a mean free path longer than their sizes.

Ozugurlu [151] fabricated $Zn_{1-x}Cd_xO$ nanoparticles with different amounts of cadmium via a sol-gel method. Williamson-Hall method was used to estimate the strain, stress and crystallite size of their samples. The results showed that up to 2% Cd doping, the crystallite size declines while the strain grows. After that, the crystallite size and strain began to oscillate as the Cd doping increased, which is a sign that the secondary phase of CdO has formed.

Kumar et al. [152] investigated the effects of Sr^{2+} doping on the

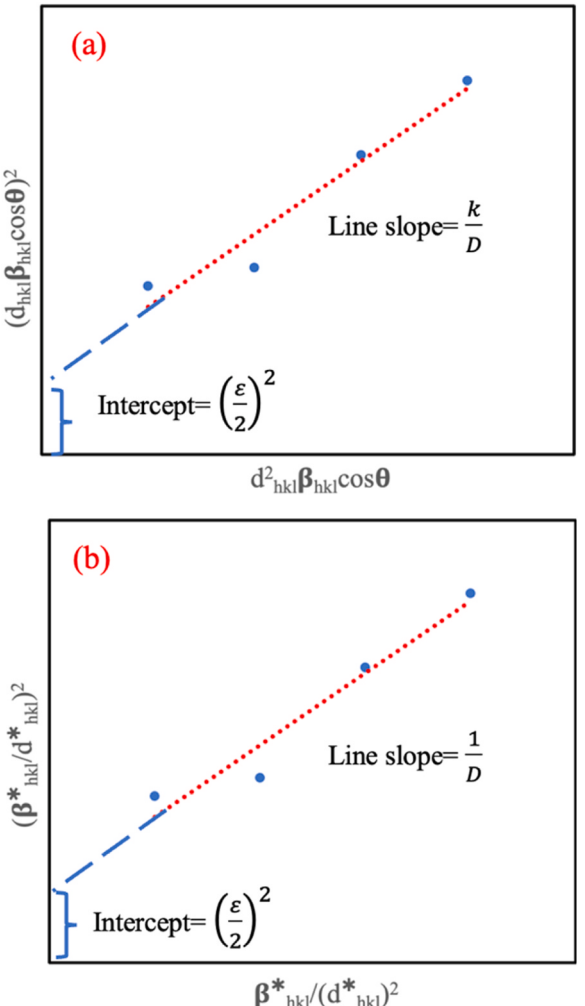


Fig. 6. Crystallite size and strain calculation via (a) Size-Strain method, and (b) Halder-Wagner approximation.

physical and optical properties of YFeO_3 perovskite phosphors. They used both Scherrer and Williamson-Hall methods to calculate crystallite size. It was reported that with the addition of Sr^{2+} ions, the average value of crystallite size drops and lattice strain increases. Because a small Y^{3+} ion with ionic radii of 0.90 Å is replaced by a big Sr^{2+} ion with ionic radii of 1.18 Å, the average lattice strain value rises with an increase in Sr^{2+} ion amounts. The crystallite size determined using the W-H plot approach is greater than the value of crystallite size obtained using the Scherrer equation. This discrepancy results from the presence of lattice strain, which is caused by crystallographic imperfections formed after strontium doping.

4.1.4. Size-strain plot method

Based on the W-H method, line broadening is supposed to be isotropic. This suggests that there was a microstrain contribution as well as isotropic diffracting domains. However, a method can give more precise results when it gives less weight to data from reflections at high angles, where the accuracy is typically poorer. The "size-strain plot" (SSP) was also proposed to evaluate the size-strain parameters in circumstances of isotropic line broadening. However, in this approach, it is deemed that the crystallite size profile obeys a Lorentzian function, and the strain profile is consistent with a Gaussian function [153]. Eq. 17 shows the size-strain approach.

$$(d_{hkl}\beta_{hkl}\cos\theta)^2 = \frac{k}{D} (d_{hkl}^2\beta_{hkl}\cos\theta) + \left(\frac{\varepsilon}{2}\right)^2 \quad (17)$$

Where K is a shape factor and it is 3/4 or 0.75 for spherical particles. For crystallite size and strain calculations, the term $(d_{hkl}\beta_{hkl}\cos\theta)^2$ is plotted with respect to $d_{hkl}^2\beta_{hkl}\cos\theta$ for all the peaks. Then, the best line should be fitted. The slope and y-intercept of the fitted line, yield the crystallite size and strain, respectively (Fig. 6a).

4.1.5. Halder-Wagner method

In real, XRD peaks are neither a Lorentzian function nor a Gaussian function, as the size broadening of the XRD peak profile in the SSP method has been assumed to be a Lorentzian function while strain broadening has been assumed to be a Gaussian function. However, the XRD peak regions match well with the Gaussian function, while their tails fall off too quickly without matching. Moreover, the tails of the profile fit quite well with the Lorentz function [154,155]. It means a better estimation is necessary to precisely calculate crystallite size. The Halder-Wagner technique is employed to get rid of this problem. This approach is based on the presumption that peak broadening is a symmetric Voigt function [139,156], which is a convolution of the Lorentzian function and Gaussian function [157]. Therefore, using the Halder-Wagner Method, the whole width at half the maximum of the physical profile for the Voigt function may be represented as Eq. 18.

$$\beta_{hkl}^2 = \beta_L \bullet \beta_{hkl} + \beta_G^2 \quad (18)$$

Where, L and G are the FWHM of Lorentzian and Gaussian functions, respectively. This method has the benefit that providing more weight to peaks in the low- and mid-angle ranges, where there is very little overlap between diffracting peaks. Now, the Halder-Wagner Method for the relationship between crystallite size and lattice strain is presented as Eq. 19.

$$\left(\frac{\beta_{hkl}^*}{d_{hkl}^*}\right)^2 = \frac{1}{D} \bullet \frac{\beta_{hkl}^*}{d_{hkl}^{*2}} + \left(\frac{\varepsilon}{2}\right)^2 \quad (19)$$

Where $\beta_{hkl}^* = \beta_{hkl}\cos\theta/\lambda$ and $d_{hkl}^* = 2d_{hkl}\sin\theta/\lambda$. Based on Eq. 19, the plot of $\left(\frac{\beta_{hkl}^*}{d_{hkl}^*}\right)^2$ versus $\frac{\beta_{hkl}^*}{d_{hkl}^{*2}}$ for each peak of the XRD pattern, gives the crystallite size and strain estimations. The average size is given by the slope of the fitted straight line, whereas the strain of nanocrystals is calculated by the intercept (Fig. 6b). Nath et al. [139] prepared

cadmium selenide nanoparticles by a chemical process using cadmium chloride and sodium hydrogen selenide precursor. They used different techniques to study the crystallite size and the strain from the XRD results. The calculated amount of strain from the Halder-Wagner plot was reported to be around 5 times more than the calculated value of strain derived from other models, despite the fact that the predicted crystallite size via the Halder-Wagner and SSP techniques was approximately identical. They reported that the contribution of the low- and mid-angle XRD data was what caused this rise in the predicted strain value. Furthermore, the lattice dislocations, which are a key factor in the enlargement of the reflection peaks at lower angles, may be responsible for the predicted greater value of strain as seen in the Halder-Wagner plot.

Lomakin et al. [158] studied the effect of hydrothermal synthesis conditions on the optical and structural properties of Bi-Fe-W-O pyrochlore system. They used the Halder-Wagner method to calculate crystallite size through the Rigaku Smart Lab Studio II software package. A SrTiO_3 single crystal was utilized as a standard sample to remove the peak broadening related to the instrument. Two groups of reflections were selected to measure the crystallite size. In the first group, the most intense peaks including 111, 400, 440, and 622 were chosen. Another group comprises the reflections relating to the groups of the crystallographic planes perpendicular to one direction, and the crystallite size measured for this group shows anisotropy. The peaks related to 111, 222, and 444 reflections were used to calculate the crystallite size in the [111] direction. The crystallite size calculated from both groups was relatively similar. The relatively small difference between the average crystallite size determined using two groups of peaks suggests that crystallites have an isotropic structure.

4.1.6. Rietveld method

Hugo Rietveld described a method for characterizing crystalline materials called "Rietveld refinement". A theoretical line profile is adjusted using the Rietveld method until it resembles the measured profile. The Rietveld approach is a full pattern fitting approach method. This indicates that a number of peaks were simultaneously analyzed to carry out the evaluation. However, it should be mentioned that Rietveld analysis can only be used when the material is known and when a model of the structure already exists. It is not a method for solving structures [159–161].

As mentioned before the benefit of this method is that it uses a whole-pattern fitting approach to calculate a powder pattern by using background description parameters, a structural model and a description of the peak shapes. Then, this calculated pattern compares with the pattern obtained from the experiment. In other words, after comparing the calculated intensity (model), to the observed intensity (sample), the difference between them is minimized by a least-squares refinement. This refinement can give valuable information about the structural and cell parameters, anisotropy, crystallite size, strain, atomic displacements, etc. In addition, this refinement is a useful and fast method for quantitative analysis for the determination of the weight percent of components in a composite or mixture. The quantitative analysis by this method is very worthwhile because the usual standard procedures for quantitative analysis of mixtures are hard and time-consuming. In recent years, the calculation of crystallite size via this method has attracted lots of attention [162–169].

Different software can be used for Rietveld refinement such as MAUD, TOPAS, GSAS-II, FullProf, etc. For this aim, it is necessary to have an XRD pattern of the sample and a calculated pattern model of the structure usually as a Crystallographic Information File (CIF) which can be obtained from reference sites like Crystallography Open Database. Therefore, first, we should know what phases exist in our sample to get their CIF information. After subjecting the experimental and calculated patterns to the software, fitting and refinement are done and the refined parameters are obtained. It is very important before doing these stages, the environment of the software is calibrated with an XRD pattern of a

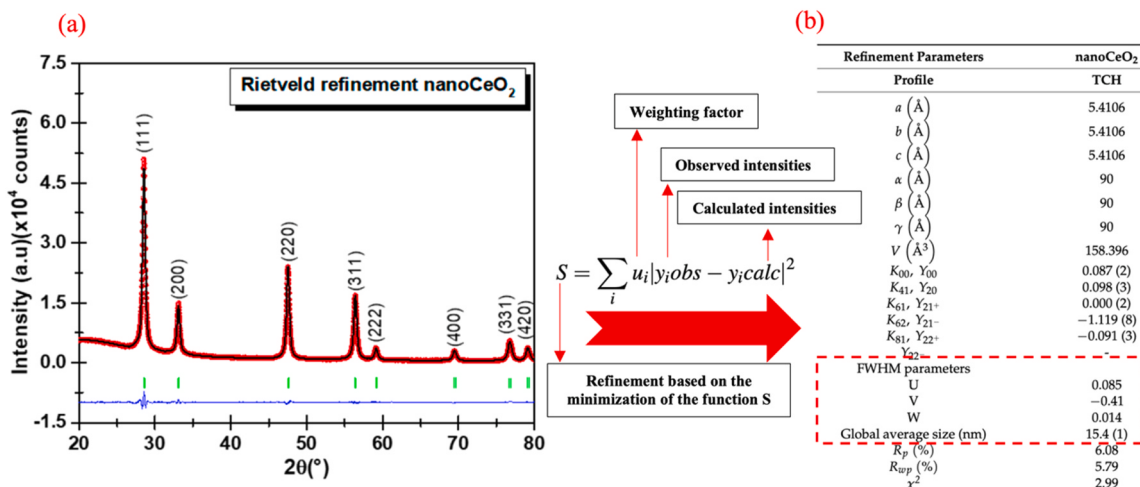


Fig. 7. (a) Rietveld refinement of cerium oxide XRD pattern using the Thompson–Cox–Hastings (TCH) function. In the XRD pattern, the black line is the calculated pattern, the observed experimental pattern is shown by the red lines, and the residual lines are presented in blue color. (b) Obtained refinement parameters including cell parameters, cell volume, crystallite size and agreement factors. Rwp and Rp are the weighted profile residual and the profile residual factors, respectively, used to verify the Rietveld refinement quality. The K are coefficients related to cerium oxide. χ^2 is the goodness of fit (Reproduced from [170]).

standard sample to consider peak width due to the instrument. Canchanya-Huaman et al. [170] investigated the grain size of CeO₂ and TiO₂ nanoparticles via various crystallite size estimation methods such as Scherrer, Williamson–Hall, size-strain plot, Halder–Wagner and Rietveld methods. They used the software FullProf Suite for the Rietveld refinement. Refinement was carried out based on the Thompson–Cox–Hastings (TCH) pseudo-Voigt function. For crystallite size estimation, Al₂O₃ standard sample was used to calibrate the software and remove the broadening from the instrument. In other words, the standard sample was employed to subtract the instrumental broadening. The Rietveld refinement results and obtained parameters are shown in Fig. 7. Based on this refinement the crystallite size of cerium oxide was estimated to be 15.4 nm. They reported that the crystallite size determined

by the Rietveld approach was close to the findings obtained by TEM, which confirmed the effectiveness of the Rietveld method in the estimation of crystallite size.

It should be emphasized that for the calculation of crystallite size and strain via Rietveld refinement, the use of a standard sample is mandatory to remove the instrumental error, and only a good data fitting does not guarantee an accurate crystallite size [171–173].

Krupa et al. [174] investigated structural changes in nanocrystalline yttrium oxide during high-energy ball milling. For the quantification of phase fraction, strain, and crystallite size, they used XRD and Rietveld refinement analyses. For this aim, a GSAS+EXPGUI refinement software package was utilized. The authors believed that although numerous approaches, including the Williamson-Hall, and their modified methods

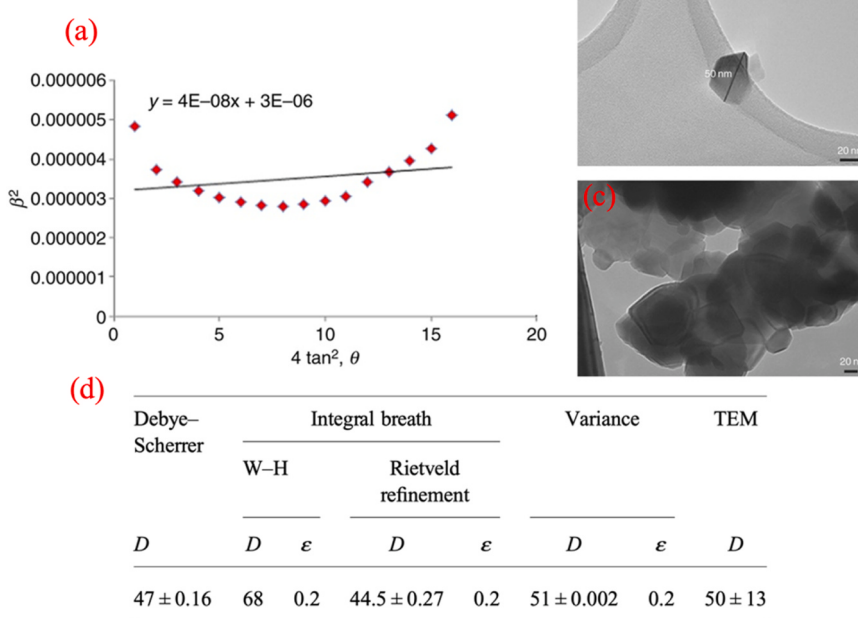


Fig. 8. (a) Variance analysis plot. (b) and (c) TEM images of the sample (bar=20 nm). (d) Obtained crystallite size (D) and strain (ε) from Scherrer, Williamson-Hall, Rietveld refinement, variance, and TEM methods [176].

can be used to determine the crystallite size, the absence of clearly resolved monoclinic yttrium oxide peaks makes the exact quantitative characterization extremely difficult. As a result, Rietveld refinement analysis would be the best technique for such cases. The Thompson-Cox-Hastings Pseudo-Voigt peak profile function was used to match the XRD patterns. This function takes into account both Gaussian and Lorentzian broadening components for the calculation of strain and crystallite size effects. The diffraction pattern of a Si standard (ICDD number 00-005-0565) was used for the calibration of peaks to refine the peak broadening related to the instrument.

4.1.7. Variance method

Variance analysis is another approach based on X-ray diffraction for calculating crystallite size and strain in nanomaterials. The method was investigated by Wilson to analyze the line broadening of the XRD peaks [72,175]. Compared to the previously mentioned methods, this approach has received less attention and there are not many results in the literature. In this method like the W-H approach the broadening is attributed to both size and strain in the sample. Based on this route, the variance 2θ coordinate is given by Eq. 20 [176].

$$\beta^2 = \frac{\lambda \Delta(2\theta)}{2\pi^2 P \cos(\theta)} + 4\tan^2\theta <\epsilon^2> \quad (20)$$

where ϵ is the strain, and P is the apparent crystallite size (nm) so that the real crystallite size is obtained by P/K (K is the shape factor). $\Delta(2\theta)$ is the angular range where the intensity of the diffraction peak is calculated (radian). For the calculation of crystallite size and strain the plot of

$\beta^2_{hkl}/\tan^2\theta$ versus $4\tan^2\theta$ should be drawn and P is given by the intercept of the fitted line, whereas ϵ is calculated by the slope (Fig. 8a). Ahmadipour et al. [176] assessed the strain and crystallite size of $\text{CaCu}_3\text{Ti}_4\text{O}_{12}$ powder synthesized by solid-state route via various estimation methods such as Rietveld refinement, Williamson-Hall, Scherrer, Variance and TEM. The plot of variance, TEM images and obtained results from their study are shown in Fig. 8. As can be seen there is a good agreement between the crystallite sizes obtained by various methods. The D value from the TEM images was about 50 nm. It should be mentioned that due to the agglomeration of the powder, it is hard to calculate a vigorous D value via TEM image for comparison with the results obtained from XRD (Fig. 8c). However, the authors believed that this value is comparable to that of Scherrer (47 nm), Rietveld refinement (44.5 nm) and Variance (51 nm) methods. There is more difference between the value from the TEM (50 nm) and the one from Williamson-Hall approximation (68 nm). The authors reported that this difference is attributed to the application of the uniform deformation model of the Williamson-Hall method, which assumed that the peak broadening is due to the isotropic contribution of strain and crystallite size. However, their real samples experienced an anisotropic strain at the grain boundary due to the presence of metal cations in $\text{CaCu}_3\text{Ti}_4\text{O}_{12}$ after sintering. According to the results of this study, it seems that the type of strain (anisotropic or isotropic strains) of the sample can influence the results in the W-H method. Therefore, based on the samples, a correct W-H model should be chosen among UDM, USDM, or UDEDHM.

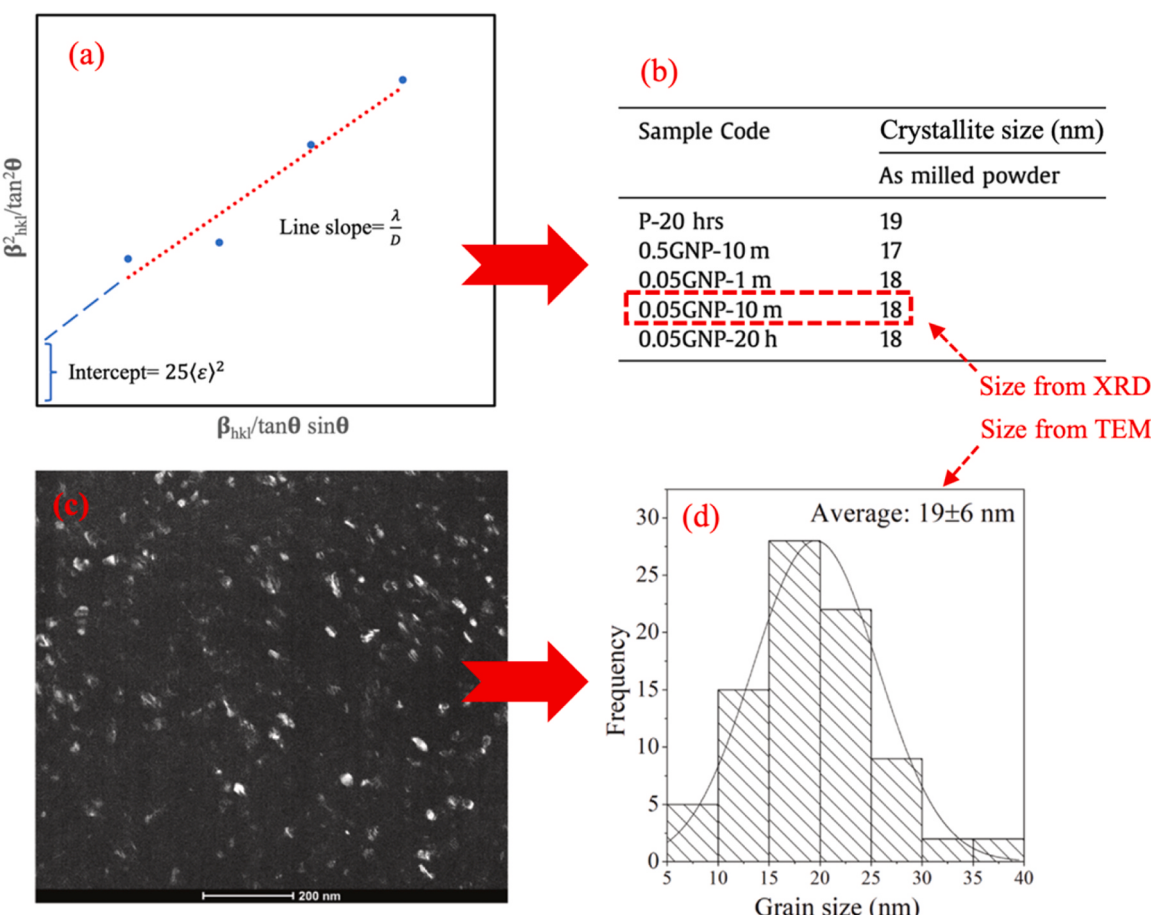


Fig. 9. (a) Proposed direct calculation procedure for Warren-Averbach method. (b) Calculated results from this approach for graphene nanoparticles (GNP)/ $\text{Bi}_2\text{Te}_{2.7}\text{Se}_{0.3}$ composites at different milling condition. (c) Dark field TEM image of the 0.05GNP/ $\text{Bi}_2\text{Te}_{2.7}\text{Se}_{0.3}$ composite (0.05GNP-10 m) with 0.05 graphene nanoparticles (bar=200 nm).

(d) Obtained crystallite size distribution from TEM image (Reproduced from ref [185]).

4.1.8. Warren-Averbach method

Warren-Averbach is another useful method for the calculation of crystallite size. In this method like W-H approach the broadening of the peak is connected to both crystallite size and strain. Other parameters like average values of the dislocation density can also be obtained by this method [177–179]. The measurements can be attained without using any assumptions about the shape of the profiles [180]. With at least two parallel reflections, the measurements are carried out by expressing the diffraction peak as a Fourier series. The method was initially utilized for use in the field of metallic materials and their alloys. However, it was rapidly extended to ceramic and polymer materials. It was reported a Gaussian function is usually used to explain strain and size-broadened peaks in this approach [181]. Based on this method, the Fourier coefficient of the peaks ($A(L)$) comprises distortion or strain ($A^D(L)$) and size ($A^S(L)$), coefficients (Eq. 21).

$$A(L) = A^D(L)A^S(L) \quad (21)$$

where L denotes the Fourier transform variable. Finally, Eq. 22 is used to determine the contribution of lattice strain and crystallite size due to the peak broadening [182].

$$\ln A(L) = \ln A^S(L) - \frac{2\pi^2 L^2 \langle \epsilon_L^2 \rangle h_0^2}{a^2} \quad (22)$$

where a is the lattice parameter. Fourier length defines as L which is equal to na_3 , n is an integer and a_3 denotes the Fourier length unit in the direction of the diffraction vector which is equal to $\frac{\lambda}{2(\sin\theta_2 - \sin\theta_1)}$. θ_2 to θ_1 is the angular diffraction width of the measured diffraction profile and λ is the wavelength of the X-ray. $h_0^2 = (h^2 + l^2 + k^2)$ and h, k, l are miller indices. $\langle \epsilon_L^2 \rangle$ is the mean square strain. L -intercept of the initial slope of the plot between $A^S(L)$ and L as it is given by the first derivative is used to determine the mean crystallite size (D) as shown in Eq. 23 [183].

$$\left[\frac{d(A^S(L))}{dL} \right]_{L=0} = \frac{-1}{D} \quad (23)$$

In addition, it was reported that the second derivative of the plot between the Fourier coefficients and L is used to calculate the crystallite size distribution [183]. This method gives average (area-weighted) crystallite size, average strain and a parameter associated with crystallite size distribution. As can be seen, this approach is not straightforward and easy. However, many commercial powder diffractometer systems offer a Warren-Averbach procedure on their software with easy-to-follow instructions. Moreover, in some studies, a direct formula was proposed for this method [184–186]. For instance, El-Makaty et al. [185] synthesized graphene/Bi₂Te_{2.7}Se_{0.3} composites via mechanical alloying and spark plasma sintered the produced powders. The crystallite size of the samples was investigated via both the Warren-Averbach approach and a dark-field TEM. They proposed Eq. 24 as the Warren-Averbach model.

$$\frac{\beta_{hkl}^2}{\tan^2\theta} = \frac{\lambda}{D} \left(\frac{\beta_{hkl}}{\tan\theta} \frac{1}{\sin\theta} \right) + 25\langle \epsilon^2 \rangle \quad (24)$$

where θ is the peak position, β_{hkl} is FHMM, ϵ is strain, D is crystallite size, and λ is the wavelength of the x-ray. For the calculation of crystallite size and strain the plot of $\frac{\beta_{hkl}^2}{\tan^2\theta}$ versus $\frac{\beta_{hkl}}{\tan\theta} \frac{1}{\sin\theta}$ should be drawn and ϵ is given by the intercept of the fitted line, whereas D is calculated by the slope (Fig. 9a). The size for as-milled powders with 0.05% graphene nanoplatelets was 18 nm (Fig. 9b). The average crystallite size of the same sample obtained from dark field TEM was about 19 nm (Fig. 9c and d). These findings confirmed a good agreement between the results obtained from this formula and TEM. However, it should be emphasized that there are not many studies that have used Eq. 24 as the Warren-Averbach model.

4.1.9. Discussion and comparing the calculation methods based on the X-Ray diffraction

Maybe the most important part to reduce the calculation error of crystallite size is the deletion of peak width caused by device error. For this aim, a coarse-grain standard sample must be used, and its width peak should be subtracted from the peak width of the tested sample via Eqs. 2 or 3.

Different techniques were proposed to measure the crystallite size from the XRD peak broadening analysis. Each of these methods has its pros and cons. The simplest method is the general Scherrer method. It is fast and facile. When the aim of a study is the comparison between results, maybe this formula is the best choice. However, as mentioned before this formula does not take into account the peak width due to strain which causes errors in the calculated crystallite size. In addition, this famous method just takes one peak for calculation. Many modifications have been made to this formula to include more peaks in the calculations. However, most of the modified Scherrer methods are not reliable, and a very wide range of results reported in the literature reduce reliance on these amendments.

To obstacle this problem more precise equations like the W-H method was proposed. The W-H equation estimates both lattice strain and crystallite size from the FWHM. Different variants of the W-H formula like the uniform deformation model, uniform stress deformation model, and uniform defect energy density model were proposed to calculate the strain more accurately. However, based on the strain in the sample, the correct form should be selected from the various W-H models. In addition, this formula does not make a difference for peaks at different diffraction angles, which reduces the accuracy of calculations.

To correct this problem, new methods such as the size-strain plot and Halder-Wagner that give weight to the peaks at different angles were proposed. Based on the reported results, the calculated crystallite sizes for both methods are relatively equal, whereas the calculated strain in the Halder-Wagner method seems to be more accurate.

The Rietveld method is a powerful and relatively accurate technique for calculating crystallite size and quantitative analysis of multiphase materials. However, in this method, data settings and user experience are crucial. For instance, many parameters can be refined without physical meaning which would lead to a good refinement but incorrect results. Therefore, the experience of the user, control and correct adjustment of refinement parameters are very important for getting accurate results.

The Warren-Averbach method, which is based on peak analysis using the Fourier series, provides relatively accurate crystallite size and lattice strain values. An important advantage of this technique compared to the previously mentioned methods is the possibility of calculating the crystallite size distribution. However, this method is not as facile, simple and straightforward as other techniques.

In general, regardless of the used calculation method, the correlation coefficient of the fitting line should be high in order to trust the results. Therefore, the first step to correctly choosing a proper calculation method is a fitted line with a good correlation coefficient. For instance, Basak et al. [187] synthesized CoFe₂O₄ nanoparticles via a co-precipitation method and used X-ray diffraction peak profile analysis to determine the crystallite size of produced powders via Scherrer, Williamson-Hall, Size-Strain Plot and Halder-Wagner methods. They analyzed the fitted graphs of all models and investigated the correlation coefficient (R^2) value in which the higher value of R^2 is more desirable (near 1). For their data, the best-fitted model was the Size-Strain Plot ($R^2 = 0.99$) which shows this method might be the best choice for their results for the calculation of crystallite size.

4.2. Calculation based on Raman spectroscopy

Raman spectroscopy is a non-destructive technique for examining chemical bonds and provides information on crystallinity, molecular interactions and chemical structure [188]. It relies on how light interacts

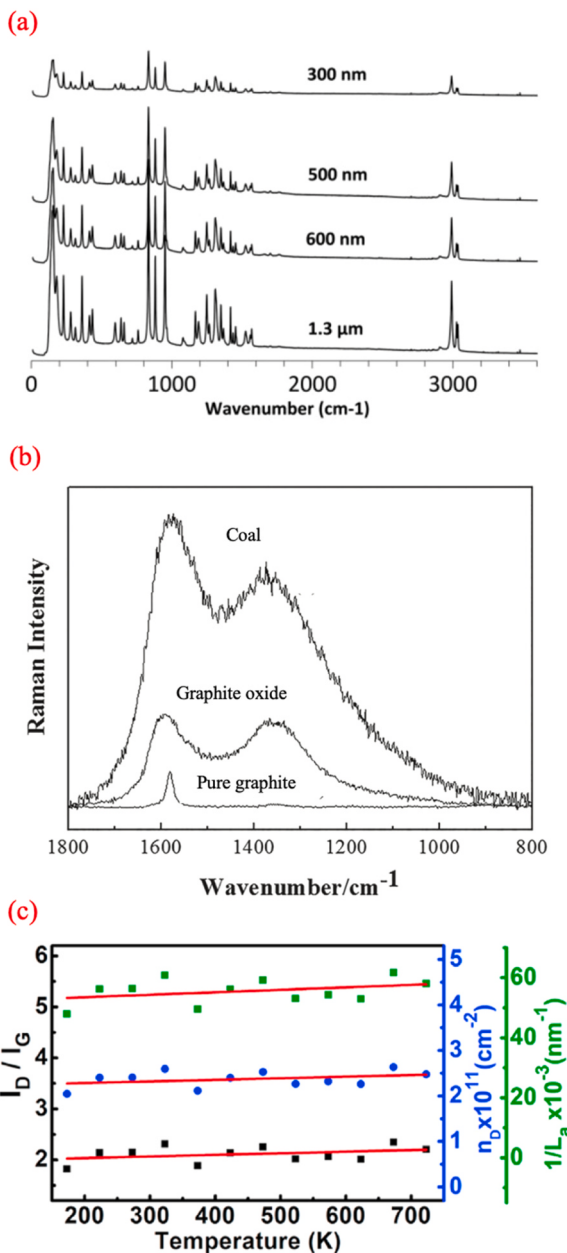


Fig. 10. (a) Raman spectra of HMX with different sizes [190], (b) Raman spectra of coal, graphite oxide, and pure graphite [203], and variation of I_D/I_G , defect density (n_D) and inverse of crystallite size (L_a) as a function of temperature [210].

with chemical bonds in the material. The basis of Raman spectroscopy is Raman scattering, commonly referred to as inelastic photon scattering [189]. Lasers in the visible, near-infrared, or near-ultraviolet range frequently emit monochromatic light. The interactions of the laser light with phonons, molecular vibrations, or other excitations in the system cause the energy of the laser photons to be pushed up or down. Information about the vibrational modes of a system is revealed by the energy shift.

Raman spectral intensity analysis allows for the detection of morphological changes, such as crystallite size [190]. For the calculation of the crystallite size via Raman spectroscopy, the intensity of the peaks should be analyzed. The intensity of the peaks for a material is a complicated phenomenon that is impacted by lots of variables. The Raman spectral parameters and specimen preparation have a significant influence on the spectral intensity. However, even if these parameters

are adequately regulated for a sample, reducing the size of the crystallites causes noticeable variations in the Raman spectra which make us possible to estimate the size [191]. This effect can be observed in Fig. 10a, which shows Raman spectroscopy of octahydro-1,3,5,7-tetranitro-1,3,5,7-tetrazocine (HMX) with different sizes [190]. As can be seen, the intensity of peaks declines with reducing crystallite size. The existence of the disordered layer at the surface of crystal may have a significant role in the observed signal attenuation and reduction in the intensity of peaks with decreasing crystal size. Compared to bulk molecules, the molecules/atoms on a crystal surface are less stable because they have fewer neighbors and are therefore more configurationally stressed [192,193]. With nanocrystals, where the surface area to volume ratio is significantly greater, the existence of this surface disorder is extremely critical. Therefore, it is assumed that the decrease in Raman intensity is a direct consequence of the alteration in the volume fraction of the disordered layer with changing crystallite size [194,195].

For a calculation of crystallite size via Raman spectroscopy, it is necessary to draw a calibration curve from the samples with definite sizes [196,197]. For this aim, the peak intensity versus crystallite size of the standard sample should be drawn. Then, it is possible to estimate the crystallite size of an experimental sample via the calibration curve. However, for carbon materials, some equations have been proposed for the estimation of crystallite size from Raman results.

Raman spectrum of a crystalline graphite features just one peak, known as G band, at a wavelength of 1580 cm⁻¹ [198]. However, an extra feature can be seen at 1350 cm⁻¹ with excitation laser energy of 2.41 eV in the specimens with some structural disorder and amorphism that breakdowns the long-range symmetry, such as finite size effects, impurities, edges, etc. [199,200]. This additional feature is typically referred to as D band [201,202]. Fig. 10b displays the Raman spectra of three carbonaceous substances (pure graphite, coal, and graphite oxide) with various ordered structures. As can be seen, the Raman peak of graphite is mainly at 1580 cm⁻¹, while no band can be seen at 1350 cm⁻¹. Due to flaws or heteroatoms, the G band and D band exist in the Raman spectra of graphite oxide and coal [203]. The correlation between the ratio of the D and G band intensities and carbon crystallinity has been studied by certain researchers [202,204,205]. The relationship between the crystallite size and the Raman intensity was later demonstrated by Knight and White [206] who summarized the Raman spectra of several graphite systems. The inverse of the crystallite size along the basal plane may be related linearly to this relationship for carbon materials. Therefore, it is possible to calculate the crystallite size of carbon materials using D and G band intensities as shown in Eq. 25 [207].

$$L_a(nm) = \frac{560}{E_l^4} \left(\frac{I_D}{I_G} \right)^{-1} \quad (25)$$

where I_G , E_l and I_D are the integrated intensity of the G band, the excitation laser energy used in the Raman experiment in eV, and the integrated intensity of the D band, respectively. Notably, the integrated intensity regions of the D and G bands are employed rather than the peak amplitude ratio.

Sharma et al. [208] investigated the temperature-dependent Raman shifts for the characteristic peaks of reduced graphene oxide (rGO). Two primary bands at 1320 cm⁻¹ (D-band) and 1580 cm⁻¹ (G-band) comprise the Raman spectra of rGO. The temperature-dependent variation of I_D/I_G is shown in Fig. 10c, and the obtained results of La are between 16 and 21 nm. It was reported that the crystallite size of rGO follows linear variation with the inverse of I_D/I_G for crystallites larger than 2 nm, whereas for crystallites smaller than 2 nm, the linear relationship breaks down, and I_D/I_G fluctuates quadratically with crystallite size. [209,210].

Gawęda et al. [211] studied the graphite structure with Raman spectroscopy. They used Eq. 26 for the calculation of crystallite size according to the band's full width at half maximum (FWHM).

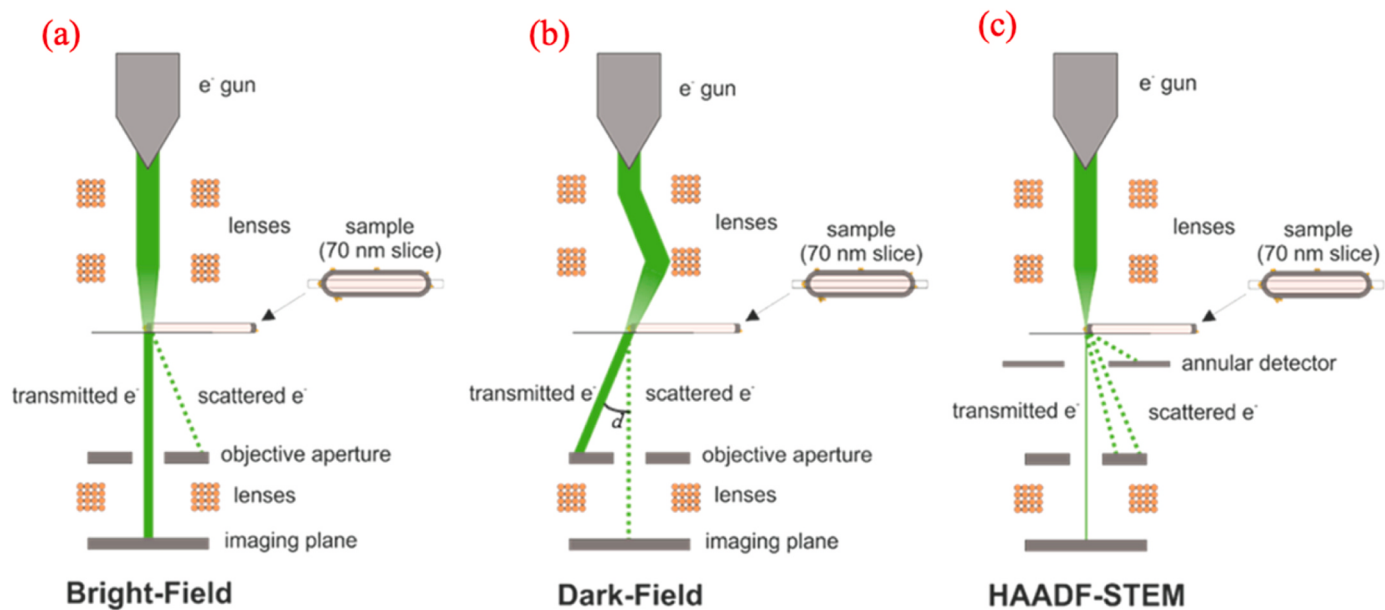


Fig. 11. Comparison of (a) bright field mode of TEM, (b) dark field mode of TEM, and (c) HAADF-STEM [221].

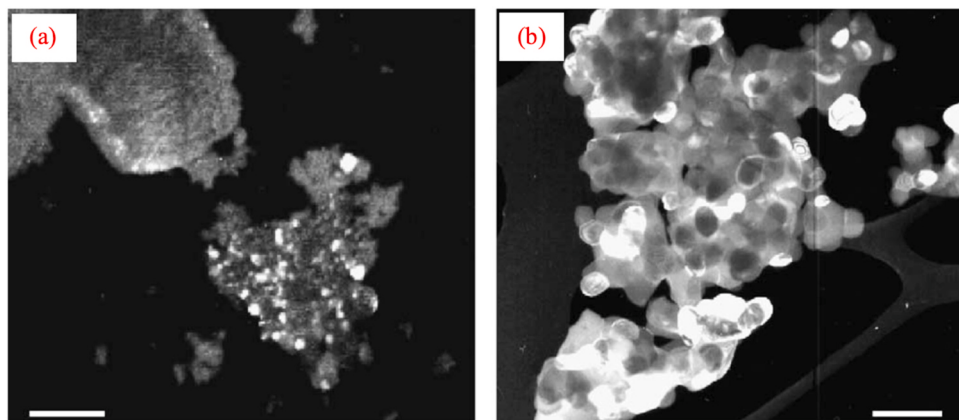


Fig. 12. Dark field TEM images of Al_2O_3 -YAG powder head-treated at 900°C (a) and 1300°C (b) for 30 min (bar=300 nm) [222].

$$L_a(\text{nm}) = \frac{l_C}{2} \ln \left[\frac{C}{\Gamma_G^A(L_A) - \Gamma_G^A(\infty)} \right] \quad (26)$$

where $\Gamma_G^A(L_A)$ and $\Gamma_G^A(\infty)$ are the FWHM of the G band and the minimum FWHM for a pure specimen, respectively. l_C and C denote the full decay length and a parameter related to the phonon dispersion, respectively. They used the reduction in crystallite size as an indicator for increasing disorder in graphite. The results showed crystallite size reduced after irradiating the samples with Ar^+ and He^+ ions.

Based on the literature review, it can be concluded that the estimation of crystallite size via Raman spectroscopy has been well documented for carbon material, whereas for other nanomaterial drawing a calibration curve is necessary which makes the calculation process time-consuming and difficult.

4.3. Calculation based on Dark-field transmission electron microscopy

For the microstructure investigation of nanomaterials, transmission electron microscopy (TEM) offers very useful results in morphology, particle size, and chemical compositions (Fig. 11). TEM is currently evolving from a basic imaging tool to a complete research toolbox, equipped with a variety of analytical modes and associated detectors,

including, energy-loss electrons, X-rays, and backscattered electrons, which not only gives microstructural data but also information about the chemical compositions of nanomaterials [212,213]. There are two important modes used for taking images by TEM which comprise bright field and dark field [214–216]. The electron populations employed to create the TEM image are the origin of the bright field or dark field mode. The most frequent images produced by TEM are bright field ones which have been widely used for traditional particle size and morphology investigation [217,218]. In this mode, the sample that absorbs or scatters electrons appears darker, while other regions that transmit electrons look brighter. The aperture in the bright field micrographs selects the transmitted electron beam while blocking the scattered electrons. However, the scattered electrons are chosen in the dark field mode, which excludes the unscattered electron beam from the aperture. As a result, the areas with materials will seem bright, while the areas without materials, such as the area surrounding the sample, would appear dark. This mode is more appropriate for the study of the crystal lattice and flaws [219,220]. A schematic comparison between dark field and bright field TEM is shown in Fig. 11 a and b [221]. Palmero et al. [222] synthesized Al_2O_3 -YAG nanopowders by a wet-chemical method and investigated the effect of sintering temperature on the produced powders. They used dark field mode to investigate the crystallite size of

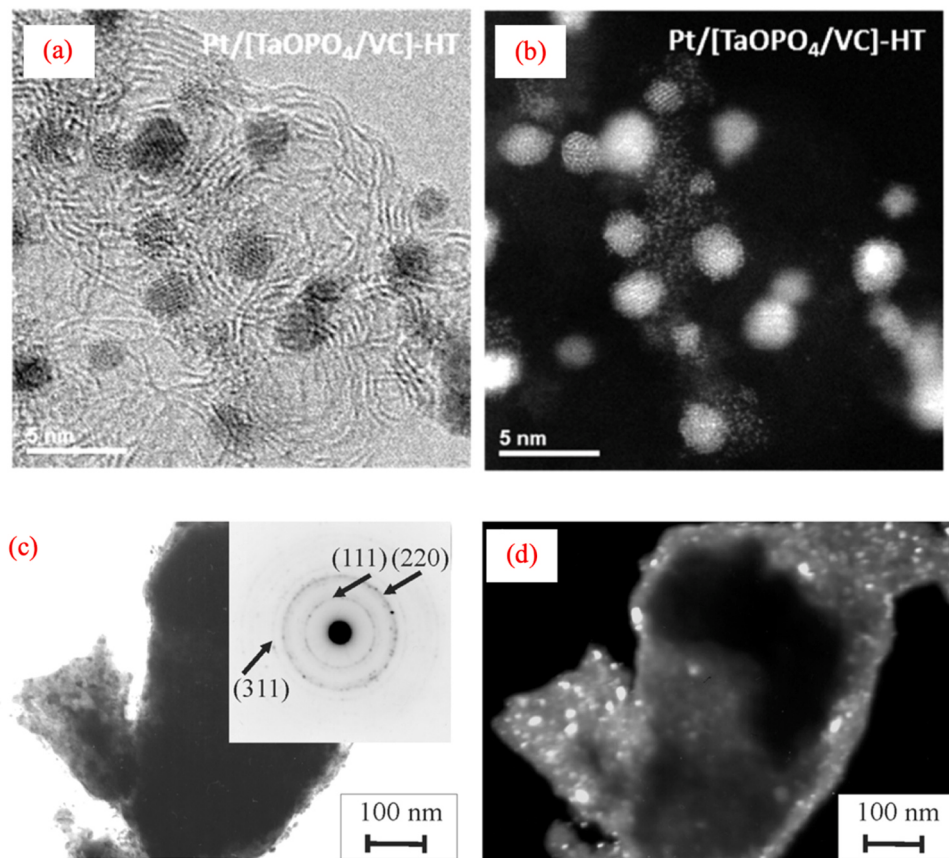


Fig. 13. (a) Bright-field image of Pt/[TaOPO₄/VC]-NHT and (b) HAADF-STEM of the same area of the sample (bar=5 nm) [227]. (c) Bright-field image of Al₂Au sample (inset: selected area diffraction pattern, SADP) and (d) dark field image in (111) Al₂Au (bar=100 nm) [229].

powders as shown in Fig. 12. As can be seen, the crystallites are clearly observed which may be the best way to calculate their sizes directly. An important advantage of this method compared to other ones is that not only the average crystallite size is obtained, but also crystallite size distribution can be measured.

The alternative imaging technique called high-angle annular dark-field imaging scanning transmission electron microscopy (HAADF-STEM), Fig. 11c, employs an annular detector to capture images of only highly scattered electrons moving through the sample. Similar to dark field light microscopy, this technique reduces image noise and produces a strong, brilliant signal for high-mass objects like nanoparticles [223]. However, the majority of HAADF detectors are positioned so that they pick up electrons dispersed by mass rather than crystallinity [221]. Therefore, in our topic, it may cause mistake results about the crystallite size and may estimate particle size. This means that caution should be applied in estimating crystallite size in this mode of TEM and maybe the dark field mode is a more reliable tool for investigating crystallites. Nevertheless, some researchers calculated crystallite size with HAADF mode. The HAADF approach can provide a comparable contrast for the cell or tissue hosting the nanoparticles since inorganic nanoparticles are frequently crystalline but biological matrices are not [224,225]. This is especially true when there are high-mass cellular components present. In addition, HAADF-STEM imaging is sensitive to high-Z atoms [226]. Epshteyn et al. [227] immobilized the catalyst Pt nanoparticles with Ta-based additives on the graphitic Vulcan carbon support. They took a bright field and HAADF images from the samples as shown in Fig. 13. Images are from an identical area of the sample, illustrating how HAADF-STEM imaging provides direct visualization of the Ta and Pt atoms. As can be seen, only platinum nanoparticles were observable in the bright field image (Fig. 13a), whereas in the HAADF-STEM micrograph, both platinum nanoparticles and tantalum atoms are directly

visualized (Fig. 13b).

In cases where the crystallite size is very small, a high-resolution transmission electron microscope (HRTEM) should be used. Although dark field images may be a useful way to investigate the crystallite size, there is not much investigation on it in the literature compared to other methods of crystallite size calculation. One limitation of this method is that in each micrograph we can have the image of the crystallites with the same crystallographic orientation. In other words, to get better results it is important to utilize different diffracted beams for getting images to have more control over all crystallographic orientations. Another limitation of this method is that it gives local information instead of a whole profile from the sample. Therefore, the best way to get comprehensive information about the crystallite size of a sample is to utilize combined techniques like XRD and TEM together. For instance, Peng et al. [228] synthesized nickel/MgH₂ nanocomposite by in-situ hydrogenolysis of nickelocene in a ball milling process. The authors used both Rietveld refinement and HRTEM for investigating the crystallite size of the samples. They compared the obtained crystallite size value from the Rietveld refinement with that calculated from HRTEM for a better understanding of the structures. Volkova et al. [229] processed a mixture of Al₂Au powder and Cu powder by a ball milling method. A solid solution of copper in the intermetallic Al₂Au phase was formed during milling which resulted in a decrease in lattice parameter. TEM images of the samples are shown in Fig. 13 c and d. The crystallite size was investigated with both XRD technique and dark-field TEM. The calculated crystallite size from diffraction peak broadening and dark-field TEM was about 20 nm and 15 nm, respectively. They reported that there is a good correlation between the obtained crystallite size results from XRD and TEM.

5. Conclusion and remarks

Precise calculation of crystallite size has been a hot debate in recent decades because this characteristic of materials has an important effect on physical, chemical, and mechanical properties. Therefore, in the present review, the studies on the precise calculation of crystallite size and their advantages and disadvantages were investigated. Several methods have been used for the approximation of crystallite size. The first and most common approach is based on the width of the peaks in the X-ray diffraction method. Several formulas with different assumptions were proposed such as Scherrer, Williamson-Hall, Size-Strain, Halder-Wagner, Rietveld, Variance, and Warren-Averbach. Some modified routes were also reported. These methods were reviewed and the calculation procedure and the source of errors were discussed. The second calculation approach was based on Raman spectroscopy which is more practical and documented for carbon-based materials. The last approach that was reviewed is a calculation based on the dark field mode of TEM or HRTEM. This method gives not only the average crystallite size with high accuracy but also provides crystallite size distribution. However, there are some limitations in this method like local information of the obtained results. Therefore, the best strategy for getting comprehensive results is to use a combined analysis of different methods because of the limitation of each method.

Declaration of Competing Interest

The authors declare that they have no known competing financial interests or personal relationships that could have appeared to influence the work reported in this paper.

Data Availability

Data will be made available on request.

References

- [1] V. Uvarov, I. Popov, Metrological characterization of X-ray diffraction methods for determination of crystallite size in nano-scale materials, *Mater. Charact.* 58 (2007) 883–891.
- [2] V. Uvarov, I. Popov, Metrological characterization of X-ray diffraction methods at different acquisition geometries for determination of crystallite size in nano-scale materials, *Mater. Charact.* 85 (2013) 111–123.
- [3] M.J. Mayo, Processing of nanocrystalline ceramics from ultrafine particles, *Int. Mater. Rev.* 41 (1996) 85–115.
- [4] N. Nithya, Synthesis and applications of ZnO nanocrystalline, *Mater. J. Optoelectron. Laser* 41 (2022) 291–301.
- [5] R. Pournajaf, S.A. Hassanzadeh-Tabrizi, Effect of heat treatment on the size, structural and catalytic properties of $\text{Al}_2\text{O}_3\text{-CeO}_2$ nanocomposite powder prepared by microemulsion method, *J. Sol.-Gel Sci. Technol.* 75 (2015) 360–365.
- [6] M.M. Motlagh, S.A. Hassanzadeh-Tabrizi, A. Saffar-Teluri, Sol-gel synthesis of $\text{Mn}_2\text{O}_3/\text{Al}_2\text{O}_3/\text{SiO}_2$ hybrid nanocomposite and application for removal of organic dye, *J. Sol.-Gel Sci. Technol.* 73 (2015) 9–13.
- [7] C.E. Kril, R. Birringer, Estimating grain-size distributions in nanocrystalline materials from X-ray diffraction profile analysis, *Philos. Mag. A* 77 (1998) 621–640.
- [8] L. Tian, L. Li, A review on the strengthening of nanostructured materials, *Int. J. Curr. Eng. Technol.* 8 (2018).
- [9] S.A. Hassanzadeh-Tabrizi, Low temperature synthesis and luminescence properties of YAG: Eu nanopowders prepared by modified sol-gel method, *Trans. Nonferrous Met. Soc. China* 21 (2011) 2443–2447.
- [10] S.A. Hassanzadeh-Tabrizi, Polymer-assisted synthesis and luminescence properties of $\text{MgAl}_2\text{O}_4\text{:Tb}$ nanopowder, *Opt. Mater. (Amst.)* 33 (2011) 1607–1609.
- [11] A. Azimi-Fouladi, P. Falak, S.A. Hassanzadeh-Tabrizi, The photodegradation of antibiotics on nano cubic spinel ferrites photocatalytic systems: A review, *J. Alloy. Compd.* (2023), 171075.
- [12] N. Baig, I. Kammakakam, W. Falath, Nanomaterials: a review of synthesis methods, properties, recent progress, and challenges, *Mater. Adv.* 2 (2021) 1821–1871.
- [13] A.A. Yaqoob, T. Parveen, K. Umar, M.N. Mohamad Ibrahim, Role of nanomaterials in the treatment of wastewater: a review, *Water* 12 (2020) 495.
- [14] C. Burda, X. Chen, R. Narayanan, M.A. El-Sayed, Chemistry and properties of nanocrystals of different shapes, *Chem. Rev.* 105 (2005) 1025–1102.
- [15] W.-N. Wang, W. Widjyastuti, T. Ogi, I.W. Lenggoro, K. Okuyama, Correlations between crystallite/particle size and photoluminescence properties of submicrometer phosphors, *Chem. Mater.* 19 (2007) 1723–1730.
- [16] P. Monisha, P. Priyadarshini, S.S. Gomathi, K. Pushpanathan, Influence of Mn dopant on the crystallite size, optical and magnetic behaviour of CoFe_2O_4 magnetic nanoparticles, *J. Phys. Chem. Solids* 148 (2021), 109654.
- [17] E. Novitskaya, J.P. Kelly, S. Bhaduri, O.A. Graeve, A review of solution combustion synthesis: an analysis of parameters controlling powder characteristics, *Int. Mater. Rev.* 66 (2021) 188–214.
- [18] C.V. Restrepo, C.C. Villa, Synthesis of silver nanoparticles, influence of capping agents, and dependence on size and shape: A review, *Environ. Nanotechnol., Monit. Manag.* 15 (2021), 100428.
- [19] S. Choopanenezhad, S.A. Hassanzadeh-Tabrizi, Synthesis of $\text{CoFe}_2\text{O}_4\text{-CaCO}_3$ nanocomposite for simultaneous magnetic hyperthermia and drug release applications, *J. Alloy. Compd.* 960 (2023), 170636.
- [20] M. Ansari, A. Bigham, S.A. Hassanzadeh Tabrizi, H. Abbastabar Ahangar, Copper-substituted spinel Zn-Mg ferrite nanoparticles as potential heating agents for hyperthermia, *J. Am. Ceram. Soc.* 101 (2018) 3649–3661.
- [21] S.K.H. Shoreh, M. Ahmadyari-Sharamin, H. Ghayour, S.A. Hassanzadeh-Tabrizi, R. Pournajaf, M. Tayebi, Two-stage synthesis of $\text{SnO}_2\text{-Ag/MgFe}_2\text{O}_4$ nanocomposite for photocatalytic application, *Surf. Interfaces* 26 (2021), 101326.
- [22] S. Upadhyay, K. Parekh, B. Pandey, Influence of crystallite size on the magnetic properties of Fe_3O_4 nanoparticles, *J. Alloy. Compd.* 678 (2016) 478–485.
- [23] A.E. Berkowitz, W.J. Schuele, P.J. Flanders, Influence of crystallite size on the magnetic properties of acicular $\gamma\text{-Fe}_2\text{O}_3$ particles, *J. Appl. Phys.* 39 (1968) 1261–1263.
- [24] M.J. Iqbal, N. Yaqub, B. Sepiol, B. Ismail, A study of the influence of crystallite size on the electrical and magnetic properties of CuFe_2O_4 , *Mater. Res. Bull.* 46 (2011) 1837–1842.
- [25] J.K. Jogi, S.K. Singhral, R. Jangir, A. Dwivedi, A.R. Tanna, R. Singh, M. Gupta, P. R. Sagdeo, Investigation of the structural and optical properties of zinc ferrite nanoparticles synthesized via a green route, *J. Electron. Mater.* 51 (2022) 5482–5491.
- [26] M.T. Ahmed, S. Islam, F. Ahmed, Comparative study on the crystallite size and bandgap of perovskite by diverse methods, *Adv. Condens. Matter Phys.* (2022) (2022).
- [27] P. Gluchowski, R. Tomala, D. Kujawa, V. Boiko, T. Murauskas, P. Solarz, Insights into the relationship between crystallite size, sintering pressure, temperature sensitivity, and persistent luminescence color of $\text{Gd}_{2-x}\text{Pr}_{x}\text{Ga}_3\text{Al}_2\text{O}_{12}$ powders and ceramics, *J. Phys. Chem. C* 126 (2022) 7127–7142.
- [28] V. Lehmann, B. Jobst, T. Muschik, A. Kux, V. Petrova-Koch, Correlation between optical properties and crystallite size in porous silicon, *Jpn. J. Appl. Phys.* 32 (1993) 2095.
- [29] S. Makhlouf, M. Kassem, M. Abdulrahim, Crystallite size dependent optical properties of nanostructured NiO films, *J. Optoelectron. Adv. Mater.* 4 (2010) 1562.
- [30] S.A. Hassanzadeh-Tabrizi, C.-C. Nguyen, T.-O. Do, Synthesis of $\text{Fe}_2\text{O}_3\text{/Pt/Au}$ nanocomposite immobilized on g-C₃N₄ for localized plasmon photocatalytic hydrogen evolution, *Appl. Surf. Sci.* 489 (2019) 741–754.
- [31] S. Mubeen, J. Lee, N. Singh, S. Krämer, G.D. Stucky, M. Moskovits, An autonomous photosynthetic device in which all charge carriers derive from surface plasmons, *Nat. Nanotechnol.* 8 (2013) 247–251.
- [32] S. Li, Z. Zhao, M. Liu, X. Liu, W. Huang, S. Sun, Y. Jiang, Y. Liu, J. Zhang, Z. Zhang, Remarkably Enhanced Photocatalytic Performance of Au/AgNbO₃ Heterostructures by Coupling Piezotronic with Plasmonic Effects, *Nano Energy* (2022), 107031.
- [33] S.A. Hassanzadeh-Tabrizi, Synthesis of NiFe₂O₄/Ag nanoparticles immobilized on mesoporous g-C₃N₄ sheets and application for degradation of antibiotics, *J. Photochem. Photobiol. A Chem.* (2021), 113398.
- [34] C. Wang, X.-G. Nie, Y. Shi, Y. Zhou, J.-J. Xu, X.-H. Xia, H.-Y. Chen, Direct plasmon-accelerated electrochemical reaction on gold nanoparticles, *ACS Nano* 11 (2017) 5897–5905.
- [35] X. Zhang, C. Huang, M. Wang, P. Huang, X. He, Z. Wei, Transient localized surface plasmon induced by femtosecond interband excitation in gold nanoparticles, *Sci. Rep.* 8 (2018) 1–7.
- [36] S. Linic, S. Chavez, R. Elias, Flow and extraction of energy and charge carriers in hybrid plasmonic nanostructures, *Nat. Mater.* 20 (2021) 916–924.
- [37] G. Schuur, Mechanism of the crystallization of high polymers, *J. Polym. Sci.* 11 (1953) 385–398.
- [38] G. Strobl, From the melt via mesomorphic and granular crystalline layers to lamellar crystallites: A major route followed in polymer crystallization? *Eur. Phys. J. E* 3 (2000) 165–183.
- [39] L. Mandelkern, The structure of crystalline polymers, *Acc. Chem. Res.* 23 (1990) 380–386.
- [40] A. Keller, A note on single crystals in polymers: evidence for a folded chain configuration, *Philos. Mag. 2* (1957) 1171–1175.
- [41] K. Uetani, T. Okada, H.T. Oyama, Crystallite size effect on thermal conductive properties of nonwoven nanocellulose sheets, *Biomacromolecules* 16 (2015) 2220–2227.
- [42] F. Guan, J. Wang, J. Pan, Q. Wang, L. Zhu, Effects of polymorphism and crystallite size on dipole reorientation in poly(vinylidene fluoride) and its random copolymers, *Macromolecules* 43 (2010) 6739–6748.
- [43] M. Jaworska, K. Sakurai, P. Gaudon, E. Guibal, Influence of chitosan characteristics on polymer properties. I: Crystallographic properties, *Polym. Int.* 52 (2003) 198–205.

- [44] J. Leisen, H.W. Beckham, M.A. Sharaf, Evolution of crystallinity, chain mobility, and crystallite size during polymer crystallization, *Macromolecules* 37 (2004) 8028–8034.
- [45] X. Lu, X. Feng, Y. Yang, J. Jiang, W. Cheng, C. Liu, M. Gopinadhan, C.O. Osuji, J. Ma, M. Elimelech, Tuning the permselectivity of polymeric desalination membranes via control of polymer crystallite size, *Nat. Commun.* 10 (2019) 1–7.
- [46] R.K. Jha, P. Bhuyan, S. Mandal, S. Pal, Insights into the role of Nb segregation on grain boundary structural transition and mechanical response in a Ni–Nb system, *Mater. Chem. Phys.* 299 (2023), 127531.
- [47] L.R.R. Nunes, H. do, P. Labaki, F.J. Caixeta, R.R. Gonçalves, Yb^{3+} influence on NIR emission from Pr^{3+} -doped spherical yttria nanoparticles for advances in NIR I and NIR II biological windows, *J. Lumin.* 241 (2022), 118485.
- [48] H.S. Ahmad, M. Ateeb, S. Noreen, M.I. Farooq, M.M.F.A. Baig, M.S. Nazar, M. F. Akhtar, K. Ahmad, A.R. Ayub, H. Shoukat, Biomimetic synthesis and characterization of silver nanoparticles from Dipterygium glaucum extract and its anti-cancerous activities, *J. Mol. Struct.* 1282 (2023), 135196.
- [49] C. Hu, Z. Zhang, H. Liu, P. Gao, Z.L. Wang, Direct synthesis and structure characterization of ultrafine CeO_2 nanoparticles, *Nanotechnology* 17 (2006) 5983.
- [50] R. Pournejaf, S.A. Hassanzadeh-Tabrizi, M. Jafari, Reverse microemulsion synthesis of CeO_2 nanopowder using polyoxyethylene (23) lauryl ether as a surfactant, *Ceram. Int.* 40 (2014) 8687–8692.
- [51] Z. Lin, G. Shao, W. Liu, Y. Wang, H. Wang, H. Wang, B. Fan, H. Lu, H. Xu, R. Zhang, In-situ TEM observations of the structural stability in carbon nanotubes, nanodiamonds and carbon nano-onions under electron irradiation, *Carbon N. Y* 192 (2022) 356–365.
- [52] L. Tang, X. Cheng, R. Wu, T. Cao, J. Lu, Y. Zhang, Z. Zhang, Monitoring the morphology evolution of $\text{LiNi}_{0.8}\text{Mn}_{0.1}\text{Co}_{0.1}\text{O}_2$ during high-temperature solid state synthesis via *in situ* SEM, *J. Energy Chem.* 66 (2022) 9–15.
- [53] S.A. Hassanzadeh-Tabrizi, Optimization of the synthesis parameters of high surface area ceria nanopowder prepared by surfactant assisted precipitation method, *Appl. Surf. Sci.* 257 (2011) 10595–10600.
- [54] X. Fu, Y. Ji, X. Cheng, C. Dong, Y. Fan, X. Li, Effect of grain size and its uniformity on corrosion resistance of rolled 316L stainless steel by EBSD and TEM, *Mater. Today Commun.* 25 (2020), 101429.
- [55] A. Bigham, A.H. Aghajanian, S. Allahdaneh, S.A. Hassanzadeh-Tabrizi, Multifunctional mesoporous magnetic Mg_2SiO_4 – CuFe_2O_4 core-shell nanocomposite for simultaneous bone cancer therapy and regeneration, *Ceram. Int.* 45 (2019) 19481–19488.
- [56] M.J. Hakimi-Tehrani, S.A. Hassanzadeh-Tabrizi, N. Koupaei, A. Saffar-Teluri, M. Rafiei, Facile thermal synthesis of $\text{g-C}_3\text{N}_4/\text{ZnO}$ nanocomposite with antibacterial properties for photodegradation of Methylene blue, *Mater. Res. Express* 8 (2021), 125002.
- [57] A.C. Dodd, A.J. McKinley, M. Saunders, T. Suzuki, Effect of particle size on the photocatalytic activity of nanoparticulate zinc oxide, *J. Nanopart. Res.* 8 (2006) 43–51.
- [58] A. Weibel, R. Bouchet, F. Boucl', P. Knauth, The big problem of small particles: a comparison of methods for determination of particle size in nanocrystalline anatase powders, *Chem. Mater.* 17 (2005) 2378–2385.
- [59] S.A. Hassanzadeh-Tabrizi, E. Taheri-Nassaj, Polyacrylamide gel synthesis and sintering of Mg_2SiO_4 : Eu^{3+} nanopowder, *Ceram. Int.* 39 (2013) 6313–6317.
- [60] F.C. De Lucia Jr, L. Giri, R.A. Pesce-Rodriguez, C.-C. Wu, S.W. Dean, T.M. Tovar, R.C. Sausa, E.R. Wainwright, J.L. Gottfried, Commercial aluminum powders, Part I: Particle size characterization and slow heating rate thermal analysis, *Powder Technol.* (2022), 117162.
- [61] D. Dhak, P. Pramanik, Particle size comparison of soft-chemically prepared transition metal (Co, Ni, Cu, Zn) aluminate spinels, *J. Am. Ceram. Soc.* 89 (2006) 1014–1021.
- [62] S. Bhattacharjee, DLS and zeta potential—what they are and what they are not? *J. Control.* Release 235 (2016) 337–351.
- [63] C. Malburet, M. Martin, L. Leclercq, J.-F. Cotte, J. Thiebaud, J.-P. Biron, J. Chamieh, H. Cottet, Optimization of limit of detection in Taylor dispersion analysis: application to the size determination of vaccine antigens, *Talanta Open* 7 (2023), 100209.
- [64] P. Lemal, A. Petri-Fink, S. Balog, Nanoparticles and taylor dispersion as a linear time-invariant system, *Anal. Chem.* 91 (2018) 1217–1221.
- [65] C. Malburet, L. Leclercq, J.-F. Cotte, J. Thiebaud, E. Bazin, M. Garinot, H. Cottet, Size and charge characterization of lipid nanoparticles for mRNA vaccines, *Anal. Chem.* 94 (2022) 4677–4685.
- [66] A.A. Bunaciu, E.G. Udrișteiu, H.Y. Aboul-Enein, X-ray diffraction: instrumentation and applications, *Crit. Rev. Anal. Chem.* 45 (2015) 289–299.
- [67] E. Saebnoori, N. Koupaei, S.A. Hassanzadeh, Tabrizi, The solution plasma synthesis, characterisation, and antibacterial activities of dispersed CuO nanoparticles, *Mater. Technol.* 37 (2022) 1–10.
- [68] S. Bakhtiarvand, S.A. Hassanzadeh Tabrizi, Polymer-assisted synthesis and characterization of nickel aluminate nanoparticles for photodegradation of methylene blue, *J. Adv. Mater. Process.* 9 (2021) 13–22.
- [69] K. Dome, E. Podgorbunskikh, A. Bychkov, O. Lomovsky, Changes in the crystallinity degree of starch having different types of crystal structure after mechanical pretreatment, *Polym. (Basel)* 12 (2020) 641.
- [70] W. Cai, R. Chen, H. Yang, H.B. Tao, H.-Y. Wang, J. Gao, W. Liu, S. Liu, S.-F. Hung, B. Liu, Amorphous versus crystalline in water oxidation catalysis: A case study of NiFe alloy, *Nano Lett.* 20 (2020) 4278–4285.
- [71] S. Ghadiri, S.A. Hassanzadeh-Tabrizi, A. Bigham, The effect of synthesis medium on structure and drug delivery behavior of CTAB-assisted sol-gel derived nanoporous calcium–magnesium–silicate, *J. Sol-Gel Sci. Technol.* 83 (2017) 229–236.
- [72] J. Il Langford, A.J.C. Wilson, Scherrer after sixty years: a survey and some new results in the determination of crystallite size, *J. Appl. Crystallogr.* 11 (1978) 102–113.
- [73] S.A. Hassanzadeh-Tabrizi, Spark plasma sintering of forsterite nanopowder and mechanical properties of sintered materials, *Ceram. Int.* 43 (2017) 15714–15718.
- [74] K. Loza, M. Heggen, M. Epple, Synthesis, structure, properties, and applications of bimetallic nanoparticles of noble metals, *Adv. Funct. Mater.* 30 (2020) 1909260.
- [75] E. Khalili, S.A. Hassanzadeh-Tabrizi, ZnO – CdO nanocomposite: microemulsion synthesis and dye removal ability, *J. Sol. -Gel Sci. Technol.* 81 (2017) 475–482.
- [76] M. Shiraishi, M. Inagaki, X-ray diffraction methods to study crystallite size and lattice constants of carbon materials, in: *Carbon Alloy*, Elsevier, 2003, pp. 161–173.
- [77] P. Saini, R. Sharma, N. Chadha, Determination of defect density, crystallite size and number of graphene layers in graphene analogues using X-ray diffraction and Raman spectroscopy, *Indian J. Pure Appl. Phys.* 55 (2017) 625–629.
- [78] R. Guinebretière, *X-ray Diffraction by Polycrystalline Materials*, John Wiley & Sons, 2013.
- [79] A. Guinier, *X-ray diffraction in crystals, imperfect crystals, and amorphous bodies*, Cour. Corp. (1994).
- [80] T. Ungar, Microstructural parameters from X-ray diffraction peak broadening, *Scr. Mater.* 51 (2004) 777–781.
- [81] S.A. Hassanzadeh-Tabrizi, D.M. Shahi, Synthesis of W/Fe co-doped $\text{g-C}_3\text{N}_4$ decorated with Au nanoparticles for photocatalytic performance, *Diam. Relat. Mater.* 134 (2023), 109791.
- [82] M.J. Hakimi-Tehrani, S.A. Hassanzadeh-Tabrizi, N. Koupaei, A. Saffar, M. Rafiei, Fabrication of Na-W Co-Doped Exfoliated $\text{G-C}_3\text{N}_4$ Nanoparticles for Methylene Blue, *Remov., J. Adv. Mater. Process.* 10 (2022) 3–11.
- [83] M. Asadi, M. Ghahari, S.A. Hassanzadeh-Tabrizi, A.M. Arabi, R. Nasiri, Studying the toxicity effects of coated and uncoated NaLuF_4 : Yb^{3+} , Tm^{3+} upconversion nanoparticles on blood factors and histopathology for Balb/C mice's tissue, *Mater. Res. Express* 6 (2020), 125421.
- [84] M. Zahedi, S.A. Hassanzadeh-Tabrizi, A. Saffar-Teluri, Sol-gel synthesis and luminescence properties of $\text{Ba}_2\text{SiO}_4:\text{Sm}^{3+}$ nanostructured phosphors, *Ceram. Int.* 44 (2018) 10169–10174.
- [85] S.A. Hassanzadeh-Tabrizi, Synthesis and characterization of nano Ce doped $\text{ZnO}/\gamma\text{-Al}_2\text{O}_3$ with improved photocatalytic activity, *J. Mater. Sci. Mater. Electron.* 28 (2017) 9528–9534.
- [86] A.K. Zak, W.H.A. Majid, M.E. Abrishami, R. Yousefi, X-ray analysis of ZnO nanoparticles by Williamson–Hall and size-strain plot methods, *Solid State Sci.* 13 (2011) 251–256.
- [87] R. Sivakami, S. Dhanuskodi, R. Karvembu, Estimation of lattice strain in nanocrystalline RuO_2 by Williamson–Hall and size–strain plot methods, *Spectrochim. Acta Part A Mol. Biomol. Spectrosc.* 152 (2016) 43–50.
- [88] R. Pillaiadugula, N. Gopalakrishnan, Crystallite size and micro-strain investigations of hydrothermally synthesized $\beta\text{-Ga}_2\text{O}_3$ by different analytical methods, *Funct. Mater. Lett.* 13 (2020) 2051018.
- [89] H. Irfan, M. Racik K, S. Anand, Microstructural evaluation of CoAl_2O_4 nanoparticles by Williamson–Hall and size–strain plot methods, *J. Asian Ceram. Soc.* 6 (2018) 54–62.
- [90] A. Kalita, M.P.C. Kalita, Williamson–Hall analysis and optical properties of small sized ZnO nanocrystals, *Phys. E Low.-Dimens. Syst. Nanostruct.* 92 (2017) 36–40.
- [91] S.A. Hassanzadeh-Tabrizi, M. Mazaheri, M. Aminzare, S.K. Sadrnezhaad, Reverse precipitation synthesis and characterization of CeO_2 nanopowder, *J. Alloy. Compd.* 491 (2010) 499–502.
- [92] S.A. Hassanzadeh-Tabrizi, E. Taheri-Nassaj, Sol-gel synthesis and characterization of Al_2O_3 – CeO_2 composite nanopowder, *J. Alloy. Compd.* 494 (2010) 289–294.
- [93] X. Pang, K. Gao, F. Luo, Y. Emirov, A.A. Levin, A.A. Volinsky, Investigation of microstructure and mechanical properties of multi-layer Cr/Cr₂O₃ coatings, *Thin Solid Films* 517 (2009) 1922–1927.
- [94] J. He, J. Ye, E.J. Lavernia, D. Matejczyk, C. Bampton, J.M. Schoenung, Quantitative analysis of grain size in bimodal powders by X-ray diffraction and transmission electron microscopy, *J. Mater. Sci.* 39 (2004) 6957–6964.
- [95] S.A. Hassanzadeh-Tabrizi, E. Taheri-Nassaj, Synthesis of high surface area Al_2O_3 – CeO_2 composite nanopowder via inverse co-precipitation method, *Ceram. Int.* 37 (2011) 1251–1257.
- [96] S. Das Bakshi, D. Sinha, S.G. Chowdhury, Anisotropic broadening of XRD peaks of α' -Fe: Williamson–Hall and Warren–Averbach analysis using full width at half maximum (FWHM) and integral breadth (IB), *Mater. Charact.* 142 (2018) 144–153.
- [97] E.S. Wibowo, B.-D. Park, Determination of crystallinity of thermosetting urea-formaldehyde resins using deconvolution method, *Macromol. Res.* 28 (2020) 615–624.
- [98] J. Clarysse, A. Moser, O. Yarema, V. Wood, M. Yarema, Size-and composition-controlled intermetallic nanocrystals via amalgamation seeded growth, *Sci. Adv.* 7 (2021) eabg1934.
- [99] Q. Li, X. Hao, Y. Gui, H. Qiu, Y. Ling, H. Zheng, M. Omran, L. Gao, J. Chen, G. Chen, Controlled sintering and phase transformation of yttria-doped tetragonal zirconia polycrystal material, *Ceram. Int.* 47 (2021) 27188–27194.
- [100] J.I. Langford, D. Loué, P. Scardi, Effect of a crystallite size distribution on X-ray diffraction line profiles and whole-powder-pattern fitting, *J. Appl. Crystallogr.* 33 (2000) 964–974.

- [101] K. Nguyen, I. Gueye, S. Leake, G. Le Rhun, P. Gergaud, N. Vaxelaire, Grain to grain heterogeneity in PZT thin films as probed by in situ biasing XRD, *J. Appl. Phys.* 133 (2023).
- [102] K. Gebresellasse, J.C. Lewis, J. Shirokoff, X-ray spectral line shape analysis of asphalt binders, *Energy Fuels* 27 (2013) 2018–2024.
- [103] Y.-H. Chin, Y. Wang, R.A. Dagle, X.S. Li, Methanol steam reforming over Pd/ZnO: Catalyst preparation and pretreatment studies, *Fuel Process. Technol.* 83 (2003) 193–201.
- [104] N. Arita-Merino, H. van Valenberg, E.P. Gilbert, E. Scholten, Quantitative phase analysis of complex fats during crystallization, *Cryst. Growth Des.* 20 (2020) 5193–5202.
- [105] B.A. Sakharov, V.A. Drits, Structural heterogeneity and crystallinity indices of natural kaolinites, *Lithol. Miner. Resour.* 58 (2023) 273–290.
- [106] S.A. Hassanzadeh-Tabrizi, H.H. Badr, S. Alizadeh, In situ synthesis of vanadium carbide–copper nanocomposite by a modified mechanochemical combustion method, *Ceram. Int.* 42 (2016) 9371–9374.
- [107] R. Pournajaf, S.A. Hassanzadeh-Tabrizi, R. Ebrahimi-Kahrizsangi, A. Alhaji, A. A. Nourbakhsh, Polycrystalline infrared-transparent MgO fabricated by spark plasma sintering, *Ceram. Int.* 45 (2019) 18943–18950.
- [108] M. Ahmadyar-Sharamin, S.A. Hassanzadeh-Tabrizi, Polyacrylamide gel synthesis, characterization, and optical properties of $\text{Co}_{1-x}\text{Ni}_x\text{Cr}_2\text{O}_4$ spinel nanopigment, *J. Sol.-Gel Sci. Technol.* 99 (2021) 534–545.
- [109] E. Yüziük, G.D. Yüziük, A. Hüttén, The effect of heat treatment on the FeCo phase in Tb-Fe-Co thin films, *J. Alloy. Compd.* 863 (2021), 158088.
- [110] M.A. Olgar, S. Erkan, R. Zan, Dependence of CZTS thin film properties and photovoltaic performance on heating rate and sulfurization time, *J. Alloy. Compd.* 963 (2023), 171283.
- [111] R.K. Basumatary, H. Basumatary, M.M. Raja, R. Brahma, S.K. Srivastava, Tuning magnetic properties of FePtCo ternary alloy thin films for magnetic storage device application, *J. Alloy. Compd.* 955 (2023), 170313.
- [112] M. Talaei, S.A. Hassanzadeh-Tabrizi, A. Saffar-Teluri, Synthesis of mesoporous $\text{CuFe}_2\text{O}_4@\text{SiO}_2$ core-shell nanocomposite for simultaneous drug release and hyperthermia applications, *Ceram. Int.* 47 (2021) 30287–30297.
- [113] M. Shabani, E. Saebnoori, S.A. Hassanzadeh-Tabrizi, H.R. Bakhsheshi-Rad, Novel synthesis of nickel ferrite magnetic nanoparticles by an in-liquid plasma, *J. Mater. Sci. Mater. Electron.* 32 (2021) 10424–10442.
- [114] S.M. Aydoghmis, S.A. Hassanzadeh-Tabrizi, A. Saffar-Teluri, Facile synthesis and investigation of $\text{NiO}-\text{ZnO}-\text{Ag}$ nanocomposites as efficient photocatalysts for degradation of methylene blue dye, *Ceram. Int.* 45 (2019) 14934–14942.
- [115] C.G. Shull, The determination of X-ray diffraction line widths, *Phys. Rev.* 70 (1946) 679.
- [116] M. Asadi, M. Ghahari, S.A. Hassanzadeh-Tabrizi, A.M. Arabi, R. Nasiri, Synthesis, characterization, and in vitro toxicity evaluation of upconversion luminescence $\text{NaLuF}_4:\text{Yb}^{3+}/\text{Tm}^{3+}$ nanoparticles suitable for medical applications, *J. Chin. Chem. Soc.* 67 (2020) 720–731.
- [117] M. Nasiri, S.A. Hassanzadeh-Tabrizi, Synthesis and Characterization of Folate-decorated Cobalt Ferrite Nanoparticles Coated with Poly (Ethylene Glycol) for Biomedical Applications, *J. Chin. Chem. Soc.* 65 (2018) 231–242.
- [118] F.T.L. Muniz, M.A.R. Miranda, C. Morilla dos Santos, J.M. Sasaki, The Scherrer equation and the dynamical theory of X-ray diffraction, *Acta Crystallogr. Sect. A Found. Adv.* 72 (2016) 385–390.
- [119] B. Abdullah, D. Tahir, Analysis of structural properties of X-ray diffraction for composite copper-activated carbon by modified Williamson-Hall and size-strain plotting methods, in: *J. Phys. (Ed.), Conf. Ser.*, IOP Publishing, 2018, p. 12007.
- [120] M. Rafizadeh-Sourki, S.A. Hassanzadeh-Tabrizi, Facile synthesis of $\text{Zn}_{0.5}\text{Ni}_{0.5}\text{Fe}_2\text{O}_4$ /carbon nanocomposite for hyperthermia and drug delivery applications, *Diam. Relat. Mater.* 125 (2022), 108993.
- [121] A. Monshi, M.R. Foroughi, M.R. Monshi, Modified Scherrer equation to estimate more accurately nano-crystallite size using XRD, *World J. Nano Sci. Eng.* 2 (2012) 154–160.
- [122] M. Rabiei, A. Palevicius, A. Monshi, S. Nasiri, A. Vilkauskas, G. Janusas, Comparing methods for calculating nano crystal size of natural hydroxyapatite using X-ray diffraction, *Nanomaterials* 10 (2020) 1627.
- [123] M.S. Hossain, M.M. Hasan, M. Mahmud, M. Bin Mobarak, S. Ahmed, Assessment of crystallite size of UV-synthesized hydroxyapatite using different model equations, *Chem. Pap.* 77 (2023) 463–471.
- [124] U. Holzwarth, N. Gibson, The Scherrer equation versus the 'Debye-Scherrer equation', *Nat. Nanotechnol.* 6 (2011) 534.
- [125] B.D. Cullity, Elements of X-ray Diffraction, Addison-Wesley Publishing, 1956.
- [126] K. He, N. Chen, C. Wang, L. Wei, J. Chen, Method for determining crystal grain size by x-ray diffraction, *Cryst. Res. Technol.* 53 (2018) 1700157.
- [127] M.A.R. Miranda, J.M. Sasaki, The limit of application of the Scherrer equation, *Acta Crystallogr. Sect. A Found. Adv.* 74 (2018) 54–65.
- [128] G. Pérez-Zúñiga, G. Herrera-Pérez, Y. Verde-Gómez, A.M. Valenzuela-Muñiz, Self-assembled ZnO-rGO nanocomposite, a solid-state transformation to control its crystallite size, *J. Alloy. Compd.* 875 (2021), 159992.
- [129] A. Goktas, S. Modanli, A. Tumbul, A. Kilic, Facile synthesis and characterization of ZnO , ZnO:Co , and ZnO:ZnO:Co nano rod-like homojunction thin films: Role of crystallite/grain size and microstrain in photocatalytic performance, *J. Alloy. Compd.* 893 (2022), 162334.
- [130] Z.-R. Yang, F.-H. Lin, J.-L. Chen, T.-F. Liang, T.-S. Yang, C.-J. Liu, Formation mechanism and antisite defects of scalable room-temperature aqueous synthesis of SnSe: Effects of the pH value on the reaction yield, mean crystallite size, chemical composition, and carrier concentration, *J. Alloy. Compd.* 857 (2021), 158250.
- [131] H. Mahajan, S.K. Godara, A.K. Srivastava, Synthesis and investigation of structural, morphological, and magnetic properties of the manganese doped cobalt-zinc spinel ferrite, *J. Alloy. Compd.* 896 (2022), 162966.
- [132] J. Wu, S. Zou, B. Wang, C. Feng, T. Yoshinobu, Enhanced acetone sensing properties of W-doped ZnFe_2O_4 electrospinning nanofibers, *J. Alloy. Compd.* 938 (2023), 168440.
- [133] F.M. Ali, Structural and optical characterization of $[(\text{PVA:PVP})-\text{Cu}^{2+}]$ composite films for promising semiconducting polymer devices, *J. Mol. Struct.* 1189 (2019) 352–359.
- [134] R. Kaur, K.P. Singh, S.K. Tripathi, Preparation and incorporation of $\text{NiSe}/\text{MoSe}_2$ nano arrays in PVA matrix for resistive switching memory, *J. Alloy. Compd.* 925 (2022), 166607.
- [135] S.A. Hassanzadeh-Tabrizi, T.-O. Do, Sol-gel synthesis and photocatalytic activity of $\text{ZnO}-\text{Ag}-\text{Sm}$ nanoparticles for water treatment, *J. Mater. Sci. Mater. Electron.* 29 (2018) 10986–10991.
- [136] D. Mohamad Shahi, S.A. Hassanzadeh-Tabrizi, A. Saffar-Teluri, Microemulsion synthesis, optical and photocatalytic properties of vanadium-doped nano ZnO , *Int. J. Appl. Ceram. Technol.* 15 (2018) 479–488.
- [137] S.A. Hassanzadeh-Tabrizi, Synthesis, characterization, and magnetic properties of NiFe_2O_4 nanoparticles, *J. Part. Sci. Technol.* 8 (2022) 79–85.
- [138] S.A. Hassanzadeh-Tabrizi, $\text{Mg}_0.\text{Ni}_{0.5}\text{Fe}_2\text{O}_4$ nanoparticles as heating agents for hyperthermia treatment, *J. Am. Ceram. Soc.* 102 (2019) 2752–2760.
- [139] D. Nath, F. Singh, R. Das, X-ray diffraction analysis by Williamson-Hall, Halder-Wagner and size-strain plot methods of CdSe nanoparticles-a comparative study, *Mater. Chem. Phys.* 239 (2020), 122021.
- [140] M.H. Baradaran-Ghadi, S.A. Hassanzadeh-Tabrizi, Mechanochemical self-explosive synthesis and characterization of $\text{Mo-V}_2\text{C}$ nanocomposite, *Ceram. Int.* 44 (2018) 5447–5452.
- [141] S.A. Hassanzadeh-Tabrizi, D. Davoodi, A.A. Beykzadeh, S. Salahshour, Fast mechanochemical combustion synthesis of nanostructured vanadium boride by a magnesiothermic reaction, *Ceram. Int.* 42 (2016) 1812–1816.
- [142] S.A. Hassanzadeh-Tabrizi, D. Davoodi, A.A. Beykzadeh, A. Chami, Fast synthesis of VC and V_2C nanopowders by the mechanochemical combustion method, *Int. J. Refract. Met. Hard Mater.* 51 (2015) 1–5.
- [143] D. Davoodi, S.A. Hassanzadeh-Tabrizi, A.H. Emami, S. Salahshour, A low temperature mechanochemical synthesis of nanostructured ZrC powder by a magnesiothermic reaction, *Ceram. Int.* 41 (2015) 8397–8401.
- [144] A.J. Prasetya, M. Rifai, H. Miyamoto, X-ray diffraction (XRD) profile analysis of pure ECAP-annealing Nickel samples, in: *J. Phys. Conf. Ser.*, IOP Publishing, 2020, p. 12113.
- [145] S. Brandstetter, P.M. Derlet, S. Van Petegem, H. Van Swygenhoven, Williamson-Hall anisotropy in nanocrystalline metals: X-ray diffraction experiments and atomistic simulations, *Acta Mater.* 56 (2008) 165–176.
- [146] C. Suryanarayana, M.G. Norton, C. Suryanarayana, M.G. Norton, X-rays and Diffraction, Springer, 1998.
- [147] V.D. Mote, Y. Purushotham, B.N. Dole, Williamson-Hall analysis in estimation of lattice strain in nanometer-sized ZnO particles, *J. Theor. Appl. Phys.* 6 (2012) 1–8.
- [148] C. Chen, P. Fan, D. Zhu, Z. Tian, H. Zhao, L. Wang, R. Peng, M. Zhong, Crack-Initiated Durable Low-Adhesion Trilayer Icephobic Surfaces with Microcone-Array Anchored Porous Sponges and Polydimethylsiloxane Cover, *ACS Appl. Mater. Interfaces* 15 (2023) 6025–6034.
- [149] M. Rabiei, A. Palevicius, A. Dashti, S. Nasiri, A. Monshi, A. Vilkauskas, G. Janusas, Measurement Modulus of elasticity related to the atomic density of planes in unit cell of crystal lattices, *Mater. (Basel)* 13 (2020) 4380.
- [150] H. Nakasawa, T. Takamatsu, K. Hayashi, Y. Miyazaki, Relationships between crystallite size and thermoelectric properties of nano-structured CrSi_2 prepared by the reduction-diffusion and spark plasma sintering methods, *J. Alloy. Compd.* 861 (2021), 157967.
- [151] E. Ozugurlu, Cd-doped ZnO nanoparticles: an experimental and first-principles DFT studies, *J. Alloy. Compd.* 861 (2021), 158620.
- [152] D. Kumar, S. Yadav, C.B. Singh, R.S. Yadav, S.B. Rai, A.K. Singh, Impact of Sr^{2+} doping on the structural, dielectric, ferroelectric and optical properties of YFeO_3 perovskite phosphor, *J. Alloy. Compd.* 945 (2023), 169286.
- [153] M.A. Tagliente, M. Massaro, Strain-driven (002) preferred orientation of ZnO nanoparticles in ion-implanted silica, *Nucl. Inst. Methods Phys. Res. Sect. B Beam Interact. Mater. Atoms* 266 (2008) 1055–1061.
- [154] N.C. Halder, C.N.J. Wagner, Separation of particle size and lattice strain in integral breadth measurements, *Acta Crystallogr.* 20 (1966) 312–313.
- [155] A. Hepp, C. Baerlocher, Learned peak shape functions for powder diffraction data, *Aust. J. Phys.* 41 (1988) 229–236.
- [156] L. Motevalizadeh, Z. Heidary, M.E. Abrishami, Facile template-free hydrothermal synthesis and microstrain measurement of ZnO nanorods, *Bull. Mater. Sci.* 37 (2014) 397–405.
- [157] D. Balzar, H. Ledbetter, Voigt-function modeling in Fourier analysis of size- and strain-broadened X-ray diffraction peaks, *J. Appl. Crystallogr.* 26 (1993) 97–103.
- [158] M.S. Lomakin, O.V. Proskurina, A.A. Sergeev, I.V. Buryanenko, V.G. Semenov, S. S. Voznesenskiy, V.V. Gusarov, Crystal structure and optical properties of the $\text{Bi}-\text{Fe}-\text{W}-\text{O}$ pyrochlore phase synthesized via a hydrothermal method, *J. Alloy. Compd.* 889 (2021), 161598.
- [159] G. Le Saoût, V. Kocabi, K. Scrivener, Application of the Rietveld method to the analysis of anhydrous cement, *Cem. Concr. Res.* 41 (2011) 133–148.
- [160] J.S.O. Evans, I.R. Evans, Structure analysis from powder diffraction data: rietveld refinement in excel, *J. Chem. Educ.* 98 (2020) 495–505.

- [161] Z. Yang, Y. Lu, X. Liu, F. Li, J. Chen, Application of high energy X-ray diffraction and Rietveld refinement in layered lithium transition metal oxide cathode materials, *Nano Res.* (2023) 1–14.
- [162] S.K. Ahmed, M.F. Mahmood, M. Arifuzzaman, M.B. Hossen, Enhancement of electrical and magnetic properties of Al^{3+} substituted CuZn nano ferrites with structural Rietveld refinement, *Results Phys.* 30 (2021), 104833.
- [163] M. Spiliopoulou, D.-P. Triandafyllidis, A. Valmas, C. Kosinas, A.N. Fitch, R.B. Von Dreele, I. Margiolas, Rietveld refinement for macromolecular powder diffraction, *Cryst. Growth Des.* 20 (2020) 8101–8123.
- [164] X. Zhou, D. Liu, H. Bu, L. Deng, H. Liu, P. Yuan, P. Du, H. Song, XRD-based quantitative analysis of clay minerals using reference intensity ratios, mineral intensity factors, Rietveld, and full pattern summation methods: A critical review, *Solid Earth Sci.* 3 (2018) 16–29.
- [165] D.L. Bish, J.E. Post, Quantitative mineralogical analysis using the Rietveld full-pattern fitting method, *Am. Mineral.* 78 (1993) 932–940.
- [166] R. Snellings, A. Bazzoni, K. Scrivener, The existence of amorphous phase in Portland cements: physical factors affecting Rietveld quantitative phase analysis, *Cem. Concr. Res.* 59 (2014) 139–146.
- [167] D. Zákutná, J. Vlček, P. Fitl, K. Nemkovský, D. Nižnanský, S. Disch, Noncollinear magnetism in nanosized cobalt chromite, *Phys. Rev. B* 98 (2018) 64407.
- [168] S. Kumar, P. Kumar, R. Gupta, V. Verma, Electromagnetic interference shielding behaviors of in-situ polymerized ferrite-polyaniline nano-composites and ferrite-polyaniline deposited fabrics in X-band frequency range, *J. Alloy. Compd.* 862 (2021), 158331.
- [169] M. Karolus, E. Lagiewka, Crystallite size and lattice strain in nanocrystalline Ni-Mo alloys studied by Rietveld refinement, *J. Alloy. Compd.* 367 (2004) 235–238.
- [170] Y. Canchanya-Huaman, A.F. Mayta-Armas, J. Pomalaya-Velasco, Y. Bendezú-Roca, J.A. Guerra, J.A. Ramos-Guivar, Strain and grain size determination of CeO_2 and TiO_2 nanoparticles: comparing integral breadth methods versus rietveld, μ -Raman, and TEM, *Nanomaterials* 11 (2021) 2311.
- [171] D. Baizar, H. Ledbetter, Accurate modeling of size and strain broadening in the Rietveld refinement: the “double-Voigt” approach, *Adv. X-Ray Anal.* 38 (1994) 397–404.
- [172] D. Balzar, N. Audebrand, M.R. Daymond, A. Fitch, A. Hewat, J.I. Langford, A. Le Bail, D. Louët, O. Masson, C.N. McCowan, Size-strain line-broadening analysis of the ceria round-robin sample, *J. Appl. Crystallogr.* 37 (2004) 911–924.
- [173] J. Lipp, R. Banerjee, M.F. Patwary, N. Patra, A. Dong, F. Girsigdies, S.R. Bare, J. R. Regalbuto, Extension of Rietveld refinement for benchtop powder XRD analysis of ultrasmall supported nanoparticles, *Chem. Mater.* 34 (2022) 8091–8111.
- [174] V.K. B.R., A. Dasgupta, C. Ghosh, S.K. Sinha, Analysis of structural transformation in nanocrystalline Y_2O_3 during high energy ball milling, *J. Alloy. Compd.* 900 (2022), 163550.
- [175] A.J.C. Wilson, On variance as a measure of line broadening in diffractometry: effect of a distribution of sizes on the apparent crystallite size, *J. Appl. Crystallogr.* 1 (1968) 194–196.
- [176] M. Ahmadipour, M.J. Abu, M.F. Ab Rahman, M.F. Ain, Z.A. Ahmad, Assessment of crystallite size and strain of $\text{CaCu}_3\text{Ti}_4\text{O}_{12}$ prepared via conventional solid-state reaction, *Micro Nano Lett.* 11 (2016) 147–150.
- [177] M. Morán, M.V. Álvarez, P. Vizcaíno, D.W. Brown, J. Santisteban, Dislocation density evolution in cold-rolled Zr-2.5%Nb pressure tubes under thermal treatments by high energy XRD and neutron TOF diffraction peak profile analysis, *J. Alloy. Compd.* 929 (2022), 167196.
- [178] C.-H. Cho, K. Son, H. Cho, Experimental analysis of deformation texture evolutions in pure Cu, Cu-37Zn, Al-6Mg, and -8Mg alloys at cold-rolling processes, *J. Alloy. Compd.* 934 (2023), 167879.
- [179] C.-H. Cho, J.-W. Lee, K.-T. Son, S.-K. Hyun, Strain rate effects on microstructure and texture evolution in cold-sheared Al-6 Mg alloys during low-temperature annealing, *J. Alloy. Compd.* 889 (2021), 161630.
- [180] B. Marinkovic, R.R. de Avillez, A. Saavedra, F.C.R. Assunção, A comparison between the Warren-Averbach method and alternate methods for X-ray diffraction microstructure analysis of polycrystalline specimens, *Mater. Res.* 4 (2001) 71–76.
- [181] J. Ghosh, S.K. Chattopadhyay, A.K. Meikap, S.K. Chatterjee, Microstructure characterization of titanium-base aluminium alloys by X-ray diffraction using Warren-Averbach and Rietveld method, *J. Alloy. Compd.* 453 (2008) 131–137.
- [182] R. Sobhanverdi, A. Akbari, In-situ synthesis and characterization of Cu/NbC, Cu/NbC-WxC, and Cu/WxC nanocomposites via mechanical alloying, *J. Alloy. Compd.* (2023), 171014.
- [183] K.M. Reddy, T.N. Rao, K. Radha, J. Joardar, Nanostructured tungsten carbides by thermochemical processing, *J. Alloy. Compd.* 494 (2010) 404–409.
- [184] A.S. Lemine, F.M. El-Makaty, H.A. Al-Ghanim, K.M. Youssef, Experimental and modeling analysis of p-type $\text{Bi}_{0.4}\text{Sb}_{1.6}\text{Te}_3$ and graphene nanocomposites, *J. Mater. Res. Technol.* 16 (2022) 1702–1712.
- [185] F.M. El-Makaty, K. Andre Mkhyoyan, K.M. Youssef, The effects of structural integrity of graphene on the thermoelectric properties of the n-type bismuth-telluride alloy, *J. Alloy. Compd.* 876 (2021), 160198.
- [186] M. Alsalam, H. Hamoudi, K.M. Youssef, The effect of graphene structural integrity on the power factor of tin selenide nanocomposite, *J. Alloy. Compd.* 872 (2021), 159584.
- [187] M. Basak, M.L. Rahman, M.F. Ahmed, B. Biswas, N. Sharmin, The use of X-ray diffraction peak profile analysis to determine the structural parameters of cobalt ferrite nanoparticles using Debye-Scherrer, Williamson-Hall, Halder-Wagner and Size-strain plot: Different precipitating agent approach, *J. Alloy. Compd.* 895 (2022), 162694.
- [188] A. Silge, K. Weber, D. Cialla-May, L. Müller-Bötticher, D. Fischer, J. Popp, Trends in pharmaceutical analysis and quality control by modern Raman spectroscopic techniques, *TrAC Trends Anal. Chem.* (2022), 116623.
- [189] R. Khodabakhshian, Raman spectroscopy for fresh fruits and vegetables, in: *Nondestruct. Qual. Assess. Tech. Fresh Fruits Veg.*, Springer, 2022, pp. 163–188.
- [190] R.B. Patel, V. Stepanov, H. Qiu, Dependence of Raman spectral intensity on crystal size in organic nano energetics, *Appl. Spectrosc.* 70 (2016) 1339–1345.
- [191] M. Eledath, M. Chandran, Raman study of BiFeO_3 nanostructures using different excitation wavelengths: effects of crystallite size on vibrational modes, *J. Phys. Chem. Solids* 172 (2023), 111060.
- [192] E. Roduner, Size matters: why nanomaterials are different, *Chem. Soc. Rev.* 35 (2006) 583–592.
- [193] D. Brown, V. Marcadon, P. Mele, N.D. Albérola, Effect of filler particle size on the properties of model nanocomposites, *Macromolecules* 41 (2008) 1499–1511.
- [194] J. Hernandez, N. Uras, J.P. Devlin, Molecular bending mode frequencies of the surface and interior of crystalline ice, *J. Chem. Phys.* 108 (1998) 4525–4529.
- [195] L. Delzeit, J.P. Devlin, V. Buch, Structural relaxation rates near the ice surface: Basis for separation of the surface and subsurface spectra, *J. Chem. Phys.* 107 (1997) 3726–3729.
- [196] C. Wang, T.J. Vickers, C.K. Mann, Direct assay and shelf-life monitoring of aspirin tablets using Raman spectroscopy, *J. Pharm. Biomed. Anal.* 16 (1997) 87–94.
- [197] K. Schenzel, S. Fischer, E. Brendler, New method for determining the degree of cellulose I crystallinity by means of FT Raman spectroscopy, *Cellulose* 12 (2005) 223–231.
- [198] E. Villa-Aleman, J.R. Darvin, M.H. Nielsen, T.M. Willey, Raman signatures of detonation soot, *J. Raman Spectrosc.* 53 (2022) 1571–1579.
- [199] B. Ali, H. Xu, R.T. Sang, I.V. Litvinuk, M. Rybachuk, Optimised diamond to graphite conversion via a metastable sp1-bonded carbon chain formation under an ultra-short femtosecond (30 fs) laser irradiation, *Carbon N. Y.* (2023).
- [200] R. Gupta, D.K. Yadav, S. Deka, V. Ganeshan, The characterization analysis of graphene, in: *Graphene Fabr. Prop. Appl.*, Springer, 2023, pp. 105–126.
- [201] F. Tuinstra, J.L. Koenig, Raman spectrum of graphite, *J. Chem. Phys.* 53 (2003) 1126–1130.
- [202] F. Tuinstra, J.L. Koenig, Characterization of graphite fiber surfaces with Raman spectroscopy, *J. Compos. Mater.* 4 (1970) 492–499.
- [203] Y. Xu, X. Chen, L. Wang, K. Bei, J. Wang, L.-M. Chou, Z. Pan, Progress of Raman spectroscopic investigations on the structure and properties of coal, *J. Raman Spectrosc.* 51 (2020) 1874–1884.
- [204] A. Cuesta, P. Dhamelincourt, J. Laureyns, A. Martínez-Alonso, J.M.D. Tascón, Comparative performance of X-ray diffraction and Raman microprobe techniques for the study of carbon materials, *J. Mater. Chem.* 8 (1998) 2875–2879.
- [205] T. Gruber, T.W. Zerda, M. Gerspacher, Raman studies of heat-treated carbon blacks, *Carbon N. Y.* 32 (1994) 1377–1382.
- [206] D.S. Knight, W.B. White, Characterization of diamond films by Raman spectroscopy, *J. Mater. Res.* 4 (1989) 385–393.
- [207] L.G. Cançado, K. Takai, T. Enoki, M. Endo, Y.A. Kim, H. Mizusaki, A. Jorio, L. N. Coelho, R. Magalhães-Paniago, M.A. Pimenta, General equation for the determination of the crystallite size L of a nanographite by Raman spectroscopy, *Appl. Phys. Lett.* 88 (2006), 163106.
- [208] M. Sharma, S. Rani, D.K. Pathak, R. Bhatia, R. Kumar, I. Sameera, Temperature dependent Raman modes of reduced graphene oxide: Effect of anharmonicity, crystallite size and defects, *Carbon N. Y.* 184 (2021) 437–444.
- [209] A.C. Ferrari, J. Robertson, Interpretation of Raman spectra of disordered and amorphous carbon, *Phys. Rev. B* 61 (2000) 14095.
- [210] A.C. Ferrari, J. Robertson, Resonant Raman spectroscopy of disordered, amorphous, and diamondlike carbon, *Phys. Rev. B* 64 (2001) 75414.
- [211] M. Gawęda, M. Wilczopolska, K. Suchorab, M. Frelek-Kozak, L. Kurpaska, J. Jagielski, Surface and in-depth structural changes in nuclear graphite irradiated with noble gases described with Raman imaging, *Nucl. Instrum. Methods Phys. Res. Sect. B Beam Interact. Mater. At.* 538 (2023) 103–109.
- [212] K.L. House, L. Pan, D.M. O’Carroll, S. Xu, Applications of scanning electron microscopy and focused ion beam milling in dental research, *Eur. J. Oral. Sci.* 130 (2022), e12853.
- [213] R.F. Egerton, M. Watanabe, Spatial resolution in transmission electron microscopy, *Micron* 160 (2022), 103304.
- [214] P. Rauwel, S. Küttinal, S. Ferdov, E. Rauwel, A review on the green synthesis of silver nanoparticles and their morphologies studied via TEM, *Adv. Mater. Sci. Eng.* (2015) (2015).
- [215] S.B. Rice, C. Chan, S.C. Brown, P. Eschbach, L. Han, D.S. Ensor, A.B. Stefaniak, J. Bonevich, A.E. Vladár, A.R.H. Walker, Particle size distributions by transmission electron microscopy: an interlaboratory comparison case study, *Metrologia* 50 (2013) 663.
- [216] S.A. Hassanzadeh-Tabrizi, S. Behbahanian, J. Amighian, Synthesis and magnetic properties of $\text{NiFe}_{2-x}\text{Sm}_x\text{O}_4$ nanopowder, *J. Magn. Magn. Mater.* 410 (2016) 242–247.
- [217] S.D. Findlay, N. Shibata, H. Sawada, E. Okunishi, Y. Kondo, Y. Ikuhara, Dynamics of annular bright field imaging in scanning transmission electron microscopy, *Ultramicroscopy* 110 (2010) 903–923.
- [218] A. Azimi-Fouladi, S.A. Hassanzadeh-Tabrizi, A. Saffar-Teluri, Sol-gel synthesis and characterization of $\text{TiO}_2\text{-CdO-Ag}$ nanocomposite with superior photocatalytic efficiency, *Ceram. Int.* 44 (2018) 4292–4297.
- [219] X. Liu, Y. Hou, M. Tang, L. Wang, Atom elimination strategy for MoS_2 nanosheets to enhance photocatalytic hydrogen evolution, *Chinese. Chem. Lett.* 34 (2023), 107499.
- [220] Y. Xu, K. Ren, T. Ren, M. Wang, Z. Wang, X. Li, L. Wang, H. Wang, Ultralow-content Pd in-situ incorporation mediated hierarchical defects in corner-etched

- Cu₂O octahedra for enhanced electrocatalytic nitrate reduction to ammonia, *Appl. Catal. B Environ.* 306 (2022), 121094.
- [221] N.D. Klein, K.R. Hurley, Z.V. Feng, C.L. Haynes, Dark field transmission electron microscopy as a tool for identifying inorganic nanoparticles in biological matrices, *Anal. Chem.* 87 (2015) 4356–4362.
- [222] P. Palmero, A. Simone, C. Esnouf, G. Fantozzi, L. Montanaro, Comparison among different sintering routes for preparing alumina-YAG nanocomposites, *J. Eur. Ceram. Soc.* 26 (2006) 941–947.
- [223] S. Utsunomiya, R.C. Ewing, Application of high-angle annular dark field scanning transmission electron microscopy, scanning transmission electron microscopy-energy dispersive X-ray spectrometry, and energy-filtered transmission electron microscopy to the characterization of nanopar, *Environ. Sci. Technol.* 37 (2003) 786–791.
- [224] U.M. Graham, R.A. Yokel, A.K. Dozier, L. Drummy, K. Mahalingam, M.T. Tseng, E. Birch, J. Fernback, Analytical high-resolution electron microscopy reveals organ-specific nanoceria bioprocessing, *Toxicol. Pathol.* 46 (2018) 47–61.
- [225] N.M. Liu, L. Miyashita, B.A. Maher, G. McPhail, C.J.P. Jones, B. Barratt, S. Thangaratnam, V. Karloukovski, I.A. Ahmed, Z. Aslam, Evidence for the presence of air pollution nanoparticles in placental tissue cells, *Sci. Total Environ.* 751 (2021), 142235.
- [226] L. Zhang, W. Shi, B. Zhang, A review of electrocatalyst characterization by transmission electron microscopy, *J. Energy Chem.* 26 (2017) 1117–1135.
- [227] A. Epshteyn, Y. Garsany, K.L. More, H.M. Meyer III, V. Jain, A.P. Purdy, K. E. Swider-Lyons, Effective strategy for improving electrocatalyst durability by adhesive immobilization of catalyst nanoparticles on graphitic carbon supports, *ACS Catal.* 5 (2015) 3662–3674.
- [228] C. Peng, Y. Li, Q. Zhang, Enhanced hydrogen desorption properties of MgH₂ by highly dispersed Ni: the role of in-situ hydrogenolysis of nickelocene in ball milling process, , *J. Alloy. Compd.* 900 (2022), 163547.
- [229] E.G. Volkova, K.A. Kozlov, B.D. Antonov, A.M. Murzakaev, V.A. Zavalishin, A. A. Livinets, V.A. Yu, Alloying of Al₂Au intermetallic compound with Cu by the ball milling technique, *J. Alloy. Compd.* 900 (2022), 163429.